Materials Advances

ROYAL SOCIETY OF CHEMISTRY

PAPER

View Article Online
View Journal | View Issue

Cite this: *Mater. Adv.*, 2024, 5, 4293

Self-cleaning formulations of mixed metal oxide-silver micro-nano structures with spiky coronae as antimicrobial coatings for fabrics and surfaces†

Ramya Prabhu B, ‡§[a] Bhamy Maithry Shenoy, ‡[b] Manish Verma,[a] Soumyashant Nayak,[c] Gopalkrishna Hegde[b] and Neena S. John *[a]

Antimicrobial coatings are essential for controlling the spread of pathogens and restricting their interface with hosts. These may be applied to masks as additional security to wearers over pore filtration or applied to surfaces that are often hand-touched, as the nanocoating can deactivate viruses irreversibly. We synthesized an antimicrobial nanoformulation containing mixed metal oxides (MMOs) of TiO_2, ZnO, SiO_2, and CuO with silver nanoparticles (MMO–Ag) capped with a cationic surfactant *via* a hydrothermal route. The developed nanoformulation possesses a high specific surface area of 73.5 $m^2 g^{-1}$. The nanoformulation exhibits excellent antimicrobial properties against Gram-negative (*E. coli*) and Gram-positive (*S. aureus*) bacteria, and bacteriophage viruses, superior to that of the spherical morphology. The minimum inhibition concentration (MIC) of the nanoformulation is 107 μg mL^{-1} against *S. aureus*. The enhanced antimicrobial properties of the spiky nanoformulation are attributed to its sharp nanometric tips that can physically puncture the cell membrane of pathogens *via* a mechano-bactericidal effect. The net attraction between the spiky MMO particle and bacteria is 10^2 times when compared to smooth MMO particles, as estimated by the modified DLVO theory. The developed nanoformulation-coated fabrics exhibit self-cleaning properties upon exposure to UV light by facilitating complete degradation of the bacteria owing to the photocatalytic component present in the nanoformulation that is enhanced by the electric field intensity near the tips, augmented by silver nanoparticles.

Received 1st November 2023,
Accepted 18th March 2024

DOI: 10.1039/d3ma00951c

rsc.li/materials-advances

Introduction

The outbreak of the COVID-19 pandemic has necessitated the design of novel antimicrobial materials to ensure contamination-free surfaces. The rise of new viruses, the re-emergence of their evolved variants and antibiotic drug-resistant bacteria pose serious threats to human beings.[1–3] The transmission of pathogens through surface contamination is an alarming sign that microbes are lurking to infect and spread to a larger population.[4,5] Nature has always inspired researchers to biomimic structures for achieving desired properties.[6,7] The unique bi-lipid-enveloped spherical morphology of SARS-CoV-2 with spiky glycoprotein projections has motivated us to design a novel antimicrobial nanomaterial with a striking morphological resemblance. Engineering drugs/proteins with spiky coronae, mimicking the physical structure of SARS-CoV-2 has shown an advantage over the spherical counterpart. Nanocarrier polymersomes decorated with receptor-binding domains (RBDs) mimicking the physical morphology of the virus have elicited a neutralizing antibody response to SARS-CoV-2 in mice.[8] Spiky metal–organic frameworks with a higher aspect ratio of nanospikes exhibit better cell attachment and quicker phagocytosis of the cell when employed as model antigen carriers as well as adjuvants.[9] Polyethyleneimine-functionalized spiky TiO_2 nanoparticles are reported to successfully deliver fluorescent siRNA into the cytosol facilitated by the sharp nanometric spikes that penetrate the cell membrane.[10] The spiky (5–10 nm) antiviral inhibitors designed by geometrical matching of the topography of influenza A virus (IAV) have exhibited efficient binding to the IAV surface than smoother ones.[11] Recently, Lulu Huang *et al.* have designed DNA-modified spiky gold nanoparticles and visualized the influence of spikes on myosin IIA recruitment at the cell membrane, improving the cellular uptake effectiveness.[12] From the above-mentioned studies reported in the literature, it is clear

[a] *Centre for Nano and Soft Matter Sciences, Shivanapura, Bengaluru 562162, India. E-mail: jsneena@cens.res.in*
[b] *Indian Institute of Science, Bengaluru 560012, India*
[c] *Theoretical Statistics and Mathematics Unit, Indian Statistical Institute, Bengaluru 560059, India*

† Electronic supplementary information (ESI) available. See DOI: https://doi.org/10.1039/d3ma00951c

‡ Equal contribution.

§ Present address: Prayoga Institute of Education Research, Bengaluru 560082, India.

that spiky structures will interact better with the biological membrane than the spherical particles.

A meticulous design of the material is required to achieve excellent antimicrobial properties. In this regard, several researchers across the globe are developing materials to prevent surface contamination by microbes using physical and chemical techniques. Various nanoformulations have recently been tested in this context.[13–15] Nanoparticles obtained by integrating polyphenols and tobramycin antibiotics have shown superior antimicrobial and antibiofilm properties.[16] Inorganic nanoformulations are the most potent antimicrobial agents due to their biocompatibility, earth abundance, and excellent antimicrobial activity against pathogens. Nanostructures of transition metals and their oxides have been investigated for their antibacterial properties. Silver and copper nanoparticles are suitable coating materials for personal protection equipment and surfaces due to their strong antibacterial and antiviral properties.[2,17] Previous research has shown that titanium, copper, zinc, and magnesium oxides are effective antimicrobials.[18–20] Superhydrophobic polyvinylidene fluoride@polydopamine TiO_2@ octadecylamine nanofibers have exhibited an excellent bacteriostasis rate $>99\%$ against *E. coli* and *S. aureus*.[21] However, a combination of metal oxides exhibits more effective antimicrobial effects than the single metal oxide. According to a patent by G. Ren *et al.*, a combination of metal oxides based on a ceramic metal oxide, a transition metal oxide, and a nanometal causes $>99\%$ damage to microbes and is more effective than a single metal oxide.[22]

The biocidal action of these metal oxides is due to their superior biochemical properties, which include the generation of reactive oxygen species, further causing protein dysfunction and photo killing.[23,24] Attempts have been made to imbue these nanoparticles with electrical charges by surface manipulation, which aids in the electrostatic inactivation of microorganisms.[25] Researchers are also looking into unique nanostructures with skewed micro-nanotopographies that can puncture microbial cells through physio-mechanical forces.[26–28] The topographical characteristics of nanoparticles, such as aspect ratio, surface roughness, and kurtosis, are crucial in determining their antimicrobial properties. Even though these nanoparticles can deactivate microbes, the regeneration of the pristine coated surface *via* decomposition of the debris of dead pathogens is also essential.[29] Consequently, self-cleaning, antimicrobial materials are vital to achieving a contamination-free surface over time without compromising its initial effectiveness since the retention of deactivated microbes can act as a fuel for the other pathogens. Despite extensive research on developing effective antimicrobials, nanoformulations with superior chemical, electrical, and mechanical antimicrobial properties have not yet been largely explored.

Additionally, a theoretical understanding of the antimicrobial mechanism of the chosen material and the influence of the designed geometry of the nanoparticle can help in optimizing the nanoparticle structure. The metal nanoparticles exert antimicrobial actions by interacting with the cell membrane followed by interference with the bacterial metabolism.[30] Further, the ions released from metals generate reactive oxygen species (ROS) that create high oxidative stress on the cell membrane, which may also change the permeability of the cell membrane. Previous studies ([30,31] and references therein) have shown that the smaller the nanoparticle size, the better the antimicrobial activity due to easier passive diffusion of nanoparticles into the cell. In many reported studies, the higher antibacterial activity of anisotropic nanostructures than the spherical or discoid structures is attributed to the surface area effect. Various structures with silver metal demonstrated a higher antimicrobial activity against *E. coli* and not with *S. aureus*; however, the reasons are not stated. Nanoparticles larger than 30 nm cannot undergo passive diffusion[31] and the mechanism here would be different. It is essential to understand the interactions between the nanostructures and the bacterial cell wall in order to explain the bactericidal mechanism.

There are different theoretical approaches that consider nanoparticle-bacterial interactions. In one of the studies that explained the improved activity of nanopillars with tapered topography, the stress on the bacterial membrane attributed to the hydrostatic pressure is considered as the main contributor to bactericidal effects. However, only the mechanical aspect is considered overlooking buoyant forces and electrostatic forces ([32] and references therein). The interaction between bacteria and nanoparticles in aqueous solutions is most commonly modelled using the Derjaguin–Landau–Verwey–Overbeek (DLVO) theory that involves a combination of van der Waals (VDW) and electrostatic double-layer (EDL) interactions. In order to account for the topography effect, surface roughness is also introduced into the model.[33,34] In the present case, we have a spiky sphere of the nanoparticle interacting with a spherical bacterium (*S. aureus*) and an ellipsoidal bacterium (*E. coli*); hence, it is necessary to consider the unique geometrical factor to determine the interaction energy.

In the present work, we have designed a self-cleaning, spiky and surface charged mixed metal oxide-Ag nanoformulation (MMO–Ag) and demonstrated its antiviral and antibacterial properties. The morphology and composition are specifically designed to introduce both physical and chemical interactions with the microbes effectively, thereby deactivating them. The MMO contains mixed metal oxides of titanium, zinc and silicon with dense nanospikes synthesized under hydrothermal conditions. The MMO is enclosed with a copper oxide coating and decorated with a small amount of silver nanoparticles to enhance its antimicrobial property further. The phosphonium ions on silver particles impart electrostatic interaction with the bacterial membrane.[35,36] Importantly, the sharp nanometric spikes of MMO–Ag can cause a superior mechano-bactericidal effect. The presence of a mixture of metal oxides aids in photodegradation and ROS generation. The nanoformulation is tested against Gram-positive and Gram-negative bacteria, and bacteriophage viruses, and it shows excellent deactivation of microbes. Furthermore, they are reusable by completely degrading pathogens upon exposure to UV light, demonstrating their self-cleaning properties. The prototypes of nanoformulation-coated face masks and sprays for surfaces are also developed. This nanoformulation can be used to coat urban realm,

hospitals, personal protective equipment, and air filters to prevent infection.

A theoretical model was developed to understand the antimicrobial activity of the spiky nanostructure using the DLVO approximation. The approximation has been earlier applied to compute interaction energy between the smooth sphere and the flat surface (1), smooth spheres (2), spiky sphere-flat surfaces (3), and smooth sphere-nanopatterned surfaces (4).[34,37–39] In the present study, we used this approach to derive the interaction energy between a spiky sphere and a smooth sphere. The theory was validated by comparing it with the results of existing calculations for two smooth spheres. The calculated interaction energy profiles between spiky and smooth spheres indicate that the structure can be tuned for optimum antimicrobial activity by varying the spike density and aspect ratio. Furthermore, the better antimicrobial effect on *S. aureus* bacteria than on *E. coli* can also be explained based on the developed theory. The self-cleaning property of the spiky MMO under UV illumination is studied using a computational model, and is attributed to the electric field enhancement near the spike tips, which is even higher in the presence of silver nanoparticles.

Experimental details

Materials

Titanium(IV) oxide bis(2,4-pentanedionate)acetylacetonate and zinc chloride ($ZnCl_2$) 99.99% were purchased from Alfa Aesar. Tetraethyl orthosilicate (TEOS; 98%) and silver nitrate ($AgNO_3$; 99.0%) were purchased from Sigma Aldrich. Oxalic acid (99.8%) from SD Fine, hexamethylenetetramine (HMTA; 99%), copper nitrate (Cu $(NO)_3$; 99%), and, potassium hydroxide (KOH; 84%) from Merck, tetrakis(hydroxymethyl)phosphonium chloride (THPC; ~80%) from Fluka, and ethanol from SD fine were also used in this study. Ultra-pure type-1 water was used throughout the reaction.

For mask fabrication, we used the nonwoven fabric of Spunbond Spunbond Meltblown Meltblown Spunbond (SSMMS) 25 GSM, meltblown (25 GSM) and hot air cotton (90–100 GSM) purchased from the local market.

Synthesis of the mixed metal oxide (MMO)

Spiky MMO structures were synthesized by a hydrothermal method. The precursors titanium acetylacetonate, zinc chloride, and tetraethyl orthosilicate were taken in a 1/1/1 molar ratio and dispersed in a water–ethanol mixture (50 : 50). Oxalic acid was then added to the solution (1/2 molar ratio of MMO/oxalic acid) and sonicated for 10 minutes followed by the addition of HMTA after obtaining a clear solution (1/2 molar ratio of MMO/HMTA) with stirring for 1 h. This solution is then poured into a Teflon-lined autoclave and heated at 180 °C for 12–18 h. The autoclave was cooled and a pale-yellow colour solid was obtained. It was further purified by centrifugation using a water–ethanol mixture. The spherical MMO was synthesized following a similar procedure except for the addition of oxalic acid.

Synthesis of the MMO–Ag formulation

MMO spiky structures were further coated with CuO by adding MMO to a $Cu(NO)_3$ aqueous solution taken in a 1/1.5 molar ratio (MMO/$Cu(NO)_3$) and stirred at 600 rpm for one hour. Subsequently, aqueous KOH was added to this solution ($Cu(NO)_3$/KOH, 1/2 molar ratio) and heated to 60 °C followed by the dropwise addition of the reducing agent tetrakis-(hydroxymethyl)phosphonium chloride (THPC; 1/3.5 molar ratio of MMO/THPC) and stirring for one hour. Finally, to obtain Ag nanoparticles on the MMO, a minimal amount of $AgNO_3$ was added to the obtained solution in a 1/0.4 molar ratio of MMO/$AgNO_3$ followed by stirring for 30 minutes. This nanoformulation was centrifuged and the powder obtained was dried at room temperature.

Characterization

The UV-vis absorption spectra of the MMO and MMO–Ag were recorded using a PerkinElmer Lambda 750 spectrophotometer by dispersing the synthesized material in ethanol. The bandgap of the synthesized material was calculated using the diffuse reflectance of the synthesized powder samples. The X-ray diffractogram (XRD) of the synthesized material was recorded using a Rigaku SmartLab diffractometer equipped with Cu Kα radiation (1.54 Å, 40 kV, and 30 mA). To obtain FT-IR spectra, pellets of MMO and MMO–Ag were made with KBr powder and the spectra were recorded using a PerkinElmer spectrum 1000 spectrometer. The morphology of the samples was analyzed using a field emission scanning electron microscope (FESEM) (TESCAN MIRA 3 LM). Transmission electron microscopic (TEM) images were acquired using a Talos F200 S at 200 kV. X-ray photoelectron spectroscopy was performed using a Thermo Fisher K-α with dual beam charge neutralization. The Brunauer–Emmett–Teller (BET) analysis was carried out to measure the specific surface area of MMO and MMO–Ag using a BELSORP MAX instrument. The samples were degassed at 200 °C for 4 h and the measurements were performed at a liquid nitrogen temperature of 77 K *via* N_2 adsorption. The specific surface area was calculated from the BET theory using the BELSORP software. The particle size and electrostatic charges of the MMO–Ag in ethanol were determined using Malvern NanoZS. The particle filtration efficiency of the designed mask was carried out by Particulate Filtration Efficiency at 0.3 microns ASTM F2299/F2299M-03:2017. The mask was tested at RH 65% ± 2% and Temp. 21 °C ± 1 °C.

Antimicrobial studies

The antibacterial activity of synthesized MMO–Ag against *S. aureus* and *E. coli* bacteria was studied by agar well diffusion, agar plate and plate count methods. Additionally, the minimum bactericidal concentration (MBC) and minimum inhibitory concentration (MIC) for *S. aureus* bacteria in the presence of MMO–Ag nanoformulations is performed by a micro dilution assay. The agar plate method was also employed to test the antibacterial activity of nanoformulation-coated meltblown nonwoven fabrics and the reusability of treated fabrics. The evaluation of the

antiviral activity of the MMO–Ag nanoformulation-coated meltblown nonwoven fabric against MS2 bacteriophage virus was tested employing a modified AATCC 100-2012 procedure. The bacterial filtration efficiency (BFE) of the designed face masks was tested using a biological aerosol of *S. aureus* following the ASTM: F 2101-19 procedure. The experimental procedures of antimicrobial studies are given below.

Agar well diffusion method

The agar well diffusion method was employed to explore the antibacterial activity of the MMO–Ag dispersions against *E. coli* and *S. aureus*. In a Petri dish, the Mueller–Hinton agar (MHA) was used to culture the bacteria. In addition, the antibacterial activity of the MMO–Ag dispersions against *Bacillus cereus* was also tested in Luria Bertani Agar media. A well of 8 mm is dug in the Petri dish and filled with 50 μL of the nanoformulation of various concentrations, *i.e.*, 2.5 mg mL^{-1}, 5 mg mL^{-1}, and 10 mg mL^{-1}. The nanoformulation was allowed to diffuse into the medium and interact with the plate freshly seeded with the test organisms. The standard antibiotic ciprofloxacin was used as a positive control.

Agar plate method

The agar plate method was used to evaluate the antibacterial property of the nanoformulation-coated meltblown fabric. Petri plates containing 20 mL MHA were seeded with a 24 h (old) culture of the microbial strains using a cotton swab. Nanoformulation-coated meltblown fabric samples were cut into rectangular pieces and placed on the plates, which were streaked with the test organisms. The plates were then incubated at 37 °C for 24 hours. The diameter of the inhibition zone was measured to calculate the antimicrobial activity.

Minimum inhibitory concentration (MIC)

The minimum inhibitory concentration (MIC) of the nanoformulation was determined by a microdilution assay. In this procedure, 50 μL of Mueller Hinton broth (MHB) was poured into each well of a 96-well microtitre plate. *S. aureus* bacterial inocula were grown in MHB media and the density of the suspension was adjusted to standard turbidity (7.5×10^5 CFU mL^{-1}). The microbial density was determined similarly to the antibacterial assay using a spectrophotometer. When the inocula had reached the required density (7.5×10^5 CFU mL^{-1}), 5 μL of the microbial suspension was added to each well from the lowest to highest nanoformulation concentration. Plates were then incubated at 37 °C for bacterial culture for 24 hours. Each well in the 96-well plates were injected with 100 mL of *p*-iodonitrotetrazolium violet (0.4 mg mL^{-1}) in water, and the plates were incubated at 37 °C for 30 minutes. The turbidity indicated bacterial growth, and the MIC was calculated in the wells with the lowest concentration of nanoformulation without any red colour. At 600 nm, the absorbance values were taken using a microplate reader.

Minimum bactericidal concentration

The minimum bactericidal concentration (MBC) was determined by a microdilution assay. MBC is performed, by not adding *p*-iodonitrotetrazolium violet dye in one lane of the concentrations used in MIC protocol. The concentrations on 96-well plates that exhibit no color change, indicating no growth, were plated on MH agar without any nanoformulation in this procedure. These plates were incubated for 18–20 hours at 37 °C. MBC is the concentration that exhibits no growth on the plate after incubation.

Plate count method

The plate count method was used for the enumeration of viable bacteria in the nutrient medium. The 24-hour-old cultures of microorganisms (*E. coli* and *S. aureus*) were adjusted in such a way to obtain 0.1 optical density (OD). Then this culture with 0.1 OD was subjected to dilutions of 1 : 20 thrice to get dilutions of 2×10^{-1}, 4×10^{-2}, and 8×10^{-3} CFU mL^{-1}. Then the final dilution of 8×10^{-3} was further diluted 1 : 10 times thrice to get dilutions of 8×10^{-4}, 8×10^{-5}, and 8×10^{-6} CFU mL^{-1}. The final dilutions of 8×10^{-4}, 8×10^{-5}, and 8×10^{-6} CFU mL^{-1} were treated with 10 mg mL^{-1} of MMO–Ag nanoformulation and the treated dilutions were incubated for 24 hours. Later, these were plated on Luria–Bertani (LB) broth agar plates to observe the colonies.

Antiviral test

Modified AATCC 100-2012 was used to test the antiviral activity of the nanoformulation-coated meltblown fabric. Fabrics coated with the nanoformulation (test) and uncoated (control) were cut into 50 mm diameter swatches and stacked. The number of swatches taken was sufficient to absorb the entire 0.5 mL liquid inoculum. To make a test inoculum, the stock virus (MS2 bacteriophage) was standardized. The test and control materials were inoculated with the MS2 bacteriophage virus and incubated for 2 hours and 24 hours in a humid atmosphere at 35 °C. Plaque assay techniques were used to determine the viral concentration at ''Time Zero'' in order to verify the target inocula.

Assay plates were incubated for 48 hours for the virus-host cell system. After the incubation period, following neutralization, the carrier suspensions were quantified to determine the levels of infectious virus survived, and the assay was scored for titre of test virus. Adequate control was implemented to verify the neutralization effectiveness of the antimicrobial agent with the neutralizer used. The percent reduction values were estimated and reported for test fabrics compared to the Time Zero enumeration.

Bacterial filtration efficiency

ASTM: F 210119 was used to test the bacterial filtration efficiency (BFE) of a fabricated face mask utilizing a biological aerosol of *S. aureus.* At a distance of 15 cm, the test sample was clamped between a cascade impactor and an aerosol chamber. The nebulizer assembly in the chamber was used to create a bacterial aerosol of *S. aureus* bacteria. A vacuum attached to a cascade impactor was used to draw aerosols of test organisms with a size of 3 microns through the test material. To assess the upstream aerosol counts, aerosols were collected from positive

control samples without any test specimen. The percentage BFE was determined as the ratio of upstream to downstream.

DLVO theory for the interaction between the spiky MMO and bacteria

The interaction between bacteria and nanoparticles in aqueous solutions can be determined using the Derjaguin–Landau–Verwey–Overbeek (DLVO) theory. According to this theory, the total energy is a sum of the van der Waals (VDW) and electrostatic double-layer (EDL) interactions. The DLVO theory assumes smooth morphologies, uniform chemical heterogeneities, and uniform surface properties such as the electric charge distribution[33] of microscopic particles in dilute solutes. The spiky spherical surface of the MMO particle was generated using the following equation:[34]

$$r(\theta,\phi) = a_1[1 + \alpha\cos(m\theta) + \beta\cos(n\phi)] \quad (1)$$

where a_1 is the radius of the sphere without ripples. (α, β) are the scaled frequencies and (m, n) are the scaled amplitudes of ripples along θ and ϕ coordinates, respectively. By varying the scaled amplitudes and frequencies, the aspect ratio and density of the spikes can be varied. To find the DLVO interaction energy between the rippled sphere (spiky MMO) and sphere/ellipsoid bacteria, the surface element integration (SEI) technique introduced by S. Bhattacharjee *et al.* was used.[38] According to the SEI technique, the curved surfaces of particles 1 and 2 are considered to be made of numerous differential elements of area ds. Each element facing each other on the two surfaces interact with an interaction energy dU given as follows:

$$\mathrm{d}U \approx (\hat{\boldsymbol{n}}_1\cdot\hat{\boldsymbol{k}}_1)(\hat{\boldsymbol{n}}_2\cdot\hat{\boldsymbol{k}}_2)E(h)\mathrm{d}s \quad (2)$$

where $\hat{\boldsymbol{n}}_1$ and $\hat{\boldsymbol{n}}_2$ are the outward unit normal to the surfaces of particles 1 and 2, respectively. $\hat{\boldsymbol{k}}_1$ and $\hat{\boldsymbol{k}}_2$ are the unit vectors directed towards the positive z-axis of each body-fixed coordinate system. The interaction energy between the two particles is thus given as follows:

$$U = \int_{S_1}\mathrm{d}U = \int_{A_1}\left(\hat{\boldsymbol{n}}_2\cdot\hat{\boldsymbol{k}}_2\right)\frac{\left(\hat{\boldsymbol{n}}_1\cdot\hat{\boldsymbol{k}}_1\right)}{\left|\hat{\boldsymbol{n}}_1\cdot\hat{\boldsymbol{k}}_1\right|}E(h)\mathrm{d}A_1 \quad (3)$$

where the first integral was performed over the actual surface of particle 1 and the second integral was performed over the projected area of particle 1 on the xy-plane, which is denoted by A_1. For the spiky sphere given using eqn (2), the differential area of the surface element is given as follows:

$$\mathrm{d}A_1 = r(\theta,\phi)^2\sin\theta\mathrm{d}\theta\mathrm{d}\phi \quad (4)$$

The outward unit normal to the surfaces ($\hat{\boldsymbol{n}}_1$, $\hat{\boldsymbol{n}}_2$) was calculated using bi-cubic interpolation in the x, y and z axes, from which the dot products ($\hat{\boldsymbol{n}}_1\cdot\hat{\boldsymbol{k}}_1$) and ($\hat{\boldsymbol{n}}_2\cdot\hat{\boldsymbol{k}}_2$) were calculated.

The interaction energy per unit area between two flat plates[38] is given as follows:

$$E(h) = -\frac{A_H}{12\pi h^2} + \frac{\epsilon_r\epsilon_0\kappa}{2}\left[\left(\psi_1{}^2 + \psi_2{}^2\right)(1-\coth(\kappa h)) + 2\psi_1\psi_2\mathrm{csch}(\kappa h)\right] \quad (5)$$

where the first and second terms represent the VDW and EDL interaction energies, respectively. For the EDL interaction, we considered the expression in the Bhattacharjee *et al.*[37] In eqn (5), A_H, ϵ_0, ϵ_r, κ, ψ_1 and ψ_2 are the effective Hamaker coefficient, dielectric permittivity of free space, relative dielectric constant of the suspending medium, inverse Debye length, surface potentials of surfaces 1 and 2, respectively. The effective Hamaker coefficient of particles 1 and 2 with the Hamaker coefficients A_1 and A_2 in the suspending medium with the Hamaker coefficient A_3 is given as follows:[31]

$$A_H = \left(\sqrt{A_1} - \sqrt{A_3}\right)\left(\sqrt{A_2} - \sqrt{A_3}\right) \quad (6)$$

The distance between the elements on the two interacting particles, h, is given as follows:

$$h = H \mp r(\theta,\phi)\cos\theta \mp a_2\cos\theta \quad (7)$$

where H is the distance between the centres of the two particles. The $\mp$ signs in eqn (7) arise based on which hemispheres of spheres 1 and 2 are considered for the interaction energy. The surface element integral can now be written explicitly as follows:

$$U = \int_0^{\pi}\int_0^{2\pi}\left(\hat{\boldsymbol{n}}_2\cdot\hat{\boldsymbol{k}}_2\right)\frac{\left(\hat{\boldsymbol{n}}_1\cdot\hat{\boldsymbol{k}}_1\right)}{\left|\hat{\boldsymbol{n}}_1\cdot\hat{\boldsymbol{k}}_1\right|}E(h)r(\theta,\phi)^2\sin\theta\mathrm{d}\theta\mathrm{d}\phi \quad (8)$$

The interaction energy between the spiky MMO particle and bacteria are obtained numerically using the trapezoidal rule for different distances of separation between the spiky MMO and bacteria.

Under the Derjaguin approximation, the interaction between two smooth spheres is given as follows:[31]

$$\begin{aligned} U &= U^{VDW} + U^{EDL}, \\ U^{VDW} &= \frac{-A_H(a_1a_2)}{6d(a_1+a_2)} \\ U^{EDL} &= \frac{\pi\epsilon_r\epsilon_0 a_1a_2\left(\zeta_1{}^2+\zeta_2{}^2\right)}{a_1+a_2}\left[\frac{2\zeta_1\zeta_2}{\zeta_1{}^2+\zeta_2{}^2}\ln\frac{1+\exp(-\kappa d)}{1-\exp(-\kappa d)} + \ln(1-\exp(-2\kappa d))\right] \end{aligned} \quad (9)$$

where a_2 is the radius of particle 2. ζ_1 and ζ_2 are the zeta potential of particles 1 and 2, respectively. d is the minimum distance between the particles. For the MMO, the Hamaker coefficient is taken as the average of the Hamaker coefficient of individual metals. The values of the Hamaker coefficient of SiO_2, ZnO, TiO_2, CuO, and silver are taken from reference[40] and have the value of 0.46×10^{-20} J, 1.89×10^{-20} J, 5.35×10^{-20} J, 3.45×10^{-20} J, and $100-400\times10^{-20}$ J, respectively. The Hamaker coefficient of water, *S. aureus* and *E. coli* are 3.7×10^{-20} J,[41] 1.9×10^{-21} J,[42] and $0.78–1.5\times10^{-20}$ J,[43] respectively. The inverse Debye–Hückel length is 729 nm for pH = 6.5.[41] For dilute solutions as in the present case, the surface potential is nearly equal to zeta potential. The zeta potential of the MMO from experiments is positive and equal to 38.83 mV. The surface potential of *S. aureus* and *E. coli* are taken as

−47 mV[44] and −40 mV, respectively. *E. coli* bacteria have a rod shape of length 2–6 μm and width 1.1–1.5 μm. However, for simplicity, we considered it as a spherical particle with a radius of 2 μm.

A MATLAB code was developed to numerically solve for the interaction energy. The simulation was carried out using COMSOL Multiphysics.

Results and discussion

The synthesis of the MMO was achieved by a hydrothermal method, and it is scalable. The titanium, zinc, and silicon precursors were chosen to synthesize mixed metal oxide nanostructures. The mixed metal oxide precursor was wisely selected by considering its antimicrobial properties and its biocompatibility. Initially, all the above-mentioned precursors were dispersed in the solvent, and a calculated amount of oxalic acid was added to the above dispersion followed by the addition of HMTA. The oxalic acid functions as a complexing agent, forming metal oxalates and facilitates the formation of the desired spiky morphology.[45,46] HMTA is added as a shape-directing surfactant, which is a weak base and slowly releases the OH^- ions under hydrothermal conditions, increasing the pH of the reaction mixture. During this process, the metal salt precursors get hydrolysed to form metal oxide nanostructures. Furthermore, the optimal concentration of HMTA facilitates in obtaining the spiky morphology of MMO, which favours anisotropic spike growth in the *c* direction.[47] The schematic of the synthesis method is shown in Fig. 1. The spiky MMO was coated with CuO and decorated with small amount of Ag particles to enrich the antimicrobial property of the nanoformulation. It was functionalized with cationic surfactant THPC to impart positive charges on the synthesized nanoparticles. THPC acts as a surfactant and the reducing agent for the reduction of silver salt. The unique composition of titanium oxide, zinc oxide, silicon dioxide, copper oxide, and silver nanoparticles with charged surfactant along with the spiky morphology is beneficial for superior antimicrobial properties as demonstrated in the following sections.

The morphology of the synthesized MMO is examined by FESEM, and is shown in Fig. 2(a) and (b). It is clear that the morphology of the MMO shows tiny spikes arising from a core structure. The spikes appear sharp with pointed edges. The size of the whole MMO nanostructures varies from 600 nm to 1.8 μm, while spikes possess nano dimensions. The TEM analysis verifies the dimensions of the spikes, which are discussed in the later section. Fig. 2(c) and (d) show low- and high-magnification images of MMO–Ag after the deposition of CuO and Ag nanoparticles. The deposited particles can be seen as bright spots on the MMO spikes and are distributed all over the MMO nanostructures. It is also clear from Fig. 2(d) that the spiky nature of the underlying MMO is retained even after CuO and Ag deposition. Spherical MMO–Ag without spikes were also prepared for control experiments, and the FESEM images are given in Fig. S1 (ESI†).

X-ray diffractogram of the spiky MMO shows the presence of mixed metal oxides of TiO_2, SiO_x and ZnO (Fig. S2(a), ESI†). The peaks at 25.2° (101), 37.9° (103), and 62.7° (213), correspond to the tetragonal anatase phase of TiO_2 (PDF no. 00-001-0562). The reflections at 36.2° (101) and 47.9° (102) indicate the presence of hexagonal ZnO (PDF no. 01-079-0206). The peaks observed at 22.0° (041) and 54.2° (505) correspond to SiO_2 (PDF no. 00-02-0242). Further, the XRD patterns of MMO–Ag after deposition of CuO and Ag in comparison with that of the MMO and the peak assignments are given in Fig. S2(b) and (c) (ESI†). Accordingly, in addition to the above-mentioned peaks due to metal oxides, we observed reflections corresponding to monoclinic CuO (PDF no. 00-048-1548) at 35.4° (11−1) and 38.9° (200) and cubic Ag (PDF no. 00-004-0783) at 38.1° (111), 44.2° (200), and 64.4° (220). The reflections corresponding to Cu_2O (PDF no. 01-077-0199) are also observed at 29.6° (110) and 42.3° (002).

TEM analysis of the bare MMO is carried out to view the morphology of the nanostructures in detail. The low and high-magnification TEM images of the MMO are shown in Fig. 3(a)–(c), and additional images are provided in Fig. S3 (ESI†). It is obvious

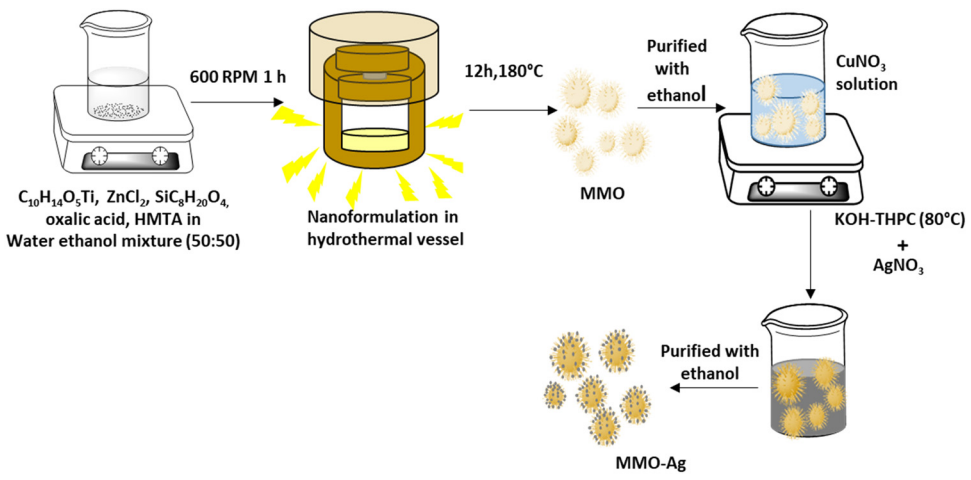

Fig. 1 Schematic diagram of the synthesis procedure for spiky MMO–Ag nanoformulations.

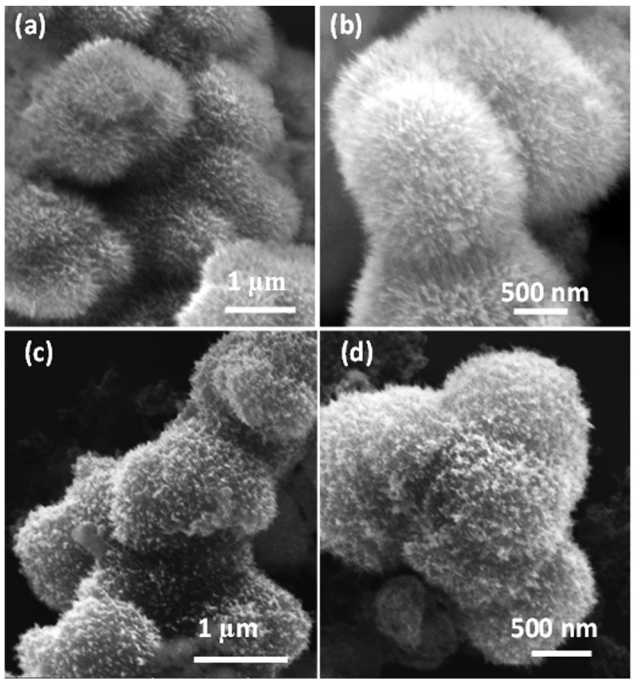

Fig. 2 FESEM images: (a) and (b) spiky MMO and (c) and (d) spiky MMO–Ag.

from the TEM images that the morphology of the MMO is radially decorated with many spikes on the surface. From Fig. 3(b), it is clear that the spikes originate from the core and are present all over the MMO structures. The spikes are 60–80 nm in length having tapered sharp tips with a diameter of 4–5 nm. The HRTEM images show lattice fringes with a *d* spacing of 0.35 nm ascribed to the (101) plane of tetragonal TiO_2 and 0.191 nm assigned to the (102) plane of hexagonal ZnO (Fig. 3(c) and Fig. S3(b), ESI†). The SAED analysis results shown in Fig. S3(c) (ESI†) indicate that the MMO exhibits a polycrystalline structure, with diffraction spots arising from TiO_2 (101), ZnO (101) and (102), and SiO_2 (514) and (502). This further supports the presence of TiO_2, ZnO, and SiO_2 phases in MMO. The morphology of the MMO has an astonishing resemblance to the coronavirus morphology, which is known for its sun-like structure with a core encapsulated with spikes. By mimicking its structure, we have envisaged a superior mechano-bactericidal effect. The energy-dispersive X-ray spectra (EDS) from TEM are given in Fig. S4 (ESI†), which show the presence of O(K), Si(K), Ti(K), and Zn(K) in 32.05 at%, 13.44 at%, 41.0 at%, and 13.50 at% for spiky MMO (before CuO and Ag deposition). Hence, MMO comprises Ti-rich oxides along with zinc and silicon oxides. The elemental mapping of the above-mentioned sample are also carried out by EDS in TEM, as shown in Fig. 3(d)–(i). The cumulative elemental map shows all the constituent elements: titanium, silicon, zinc, and oxygen. This excludes any particular metal oxide aggregation in any of the regions. It is interesting to note that the high-angle annular dark-field (HAADF) image also reveals corona spikes in accordance with the morphological studies (Fig. 3(i)).

Fig. 4 displays the TEM image of MMO–Ag structures (after the deposition of CuO and Ag). In the bright field TEM image of MMO–Ag, the deposited aggregates of CuO and silver nanoparticles appear as dark spots on MMO due to a high scattering coefficient (Fig. 4(a)). A magnified image of the spiky portion of MMO–Ag is shown in Fig. S5(a) (ESI†). The spikes of MMO–Ag structures are clearly visible at the edges decorated with spherical silver nanoparticles of a diameter ranging from 10 to 20 nm. Fig. 4(b) shows the HRTEM images of MMO–Ag and the interplanar spacings corresponding to the various components: 0.35 nm of anatase TiO_2 (101), 0.27 nm of monoclinic CuO (110), 0.30 nm of cubic Cu_2O (110), and 0.23 nm of cubic Ag (111) are observed. The EDS spectra from TEM shown in Fig. S5(b, c) (ESI†) confirm that the synthesized material contains Ti, Si, Zn, O, Cu, and Ag elements. In the interest of understanding the distribution and interface of silver nanoparticles with MMO, HAADF and TEM-EDS mapping images are provided in Fig. 4(c)–(j). The silver nanoparticles are seen as bright spots in the HAADF image and MMO appears less bright (Fig. 4(d)). The TEM-EDS mapping of MMO–Ag was performed for Ti (K), Si (K), Zn (K), O(K), Cu (K) and Ag (L) levels (Fig. 4(e)–(j)). A rather uniform distribution of Ti, Si, Zn, O, and Cu is seen from the mapping images, though the signals from the Zn level are slightly lesser than that from other elements. The TEM-EDS mapping depicts that CuO and Ag incorporation throughout the MMO surface is successful (Fig. 4(i) and (j)).

The FTIR spectra of MMO and MMO–Ag are shown in Fig. 5(a) and (b). In the FTIR spectra of MMO, a broad band is located around 3392 cm^{-1} corresponding to the stretching vibration of the O–H bond from water molecules. The peak at 1614 cm^{-1} corresponds to the bending vibration of water molecules coupled with Ti–OH vibrations and the band at 470 cm^{-1} corresponds to the vibration frequencies Ti–O–Ti.[48] The bands at 1463 and 1314 cm^{-1} can be assigned to the $-CH_2$ bending vibration of HMTA. The bands corresponding to silicon dioxide are seen at 1104 and 796 cm^{-1} due to the vibrations of Si–O–Si and Si–O, respectively.[49] The bands at 912 cm^{-1} may be assigned to C–N stretching of HMTA. The characteristic peak of the Zn–O stretching vibration is observed at 550 cm^{-1}.[50] In the case of MMO–Ag, the absorption at 3426 and 3280 cm^{-1} can be assigned to O–H stretching of water and THPC. The bands around 2900 and 1320 cm^{-1} correspond to the stretching and bending vibrations of $-CH_2$ from THPC. The pronounced peaks located around 1088 and 528 cm^{-1} are due to the vibration of the Cu–O bond.[51] A less intense band at 815 cm^{-1} corresponding to the phosphorus-carbon stretching vibration appears due to the THPC molecules.[52]

X-ray photoelectron spectroscopy (XPS) is performed to understand the surface composition of MMO (Fig. S6, ESI†) and MMO–Ag (Fig. S7 and S8, ESI†). MMO exhibits Ti 2p peaks ($2p_{3/2}$ (458.6 eV) and $2p_{1/2}$ (464.4 eV)) corresponding to Ti^{4+} in TiO_2, Zn 2p (1022.1 eV ($2p_{3/2}$) and 1045.1 eV ($2p_{1/2}$)) corresponding to Zn^{2+} in ZnO and Si 2p corresponding to Si^{2+} (103.5 eV) of SiO_2 along with low-valent Si (102.4) from SiO_x. The presence of a highly intense low-valent Si denotes the presence of a large amount of non-stoichiometric contents. The C 1s spectra exhibit features due to C–C (284.5 eV), C–N (286 eV) and O–C=O (288.4 eV) arising from sp^2 carbon, HMTA

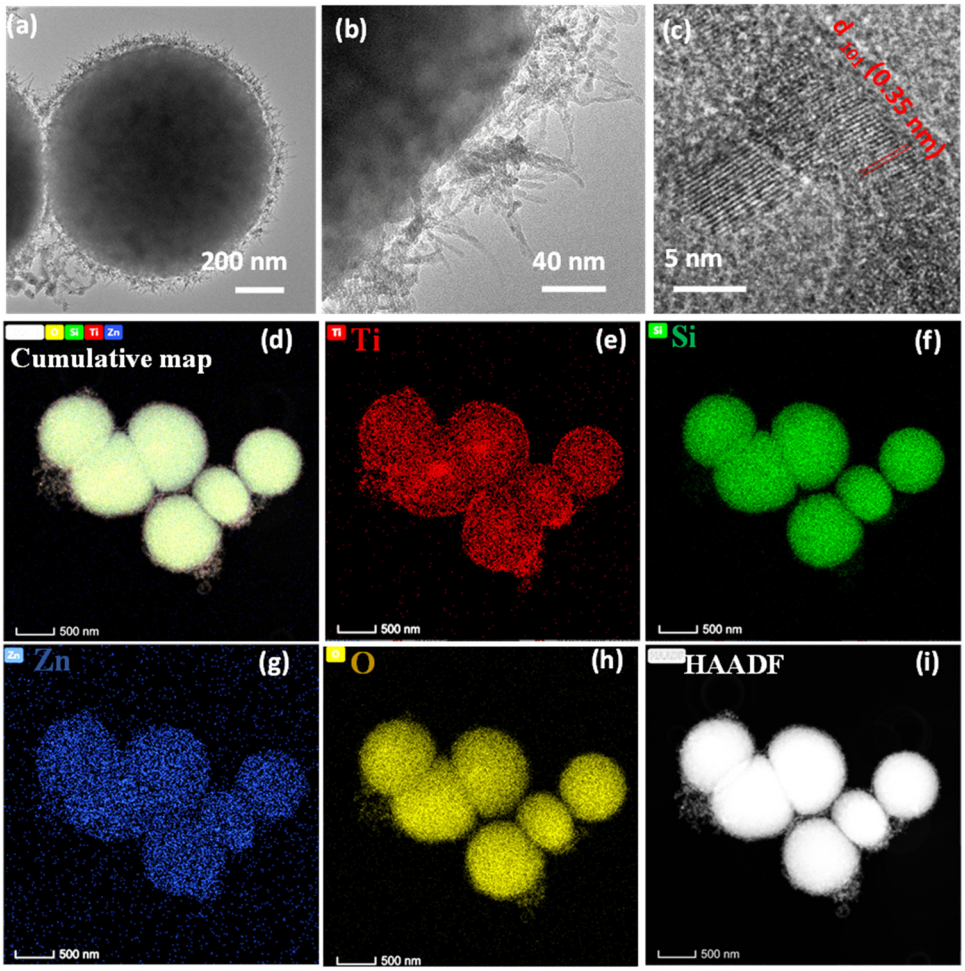

Fig. 3 (a) and (b) TEM images of the spiky MMO. (c) Magnified image of the MMO spiky tip. EDS compositional elemental mapping images of the spiky MMO: (d) cumulative map, (e) Ti K, (f) Si K, (g) Zn K, (h) O K, and (i) HAADF.

and oxalate, respectively. In the case of MMO–Ag (Fig. S7 and S8, ESI†), after subjecting to chemical reactions in KOH and reduction treatment in alkaline THPC for subsequent CuO and Ag deposition, a small amount of suboxides of Ti (460.1 eV) are observed in addition to TiO_2. For Zn 2p, in addition to ZnO features, high binding energy peaks (1025.8 and 1048.8 eV) are observed that might arise from Zn coordination to surfactants. The signatures of SiO_x (102.3 eV) as major components along with SiO_2 (103.5 eV) are observed in this case as well. Cu 2p spectra show peaks due to Cu^{1+} and Cu^{2+} (932.3 eV, 934.5 eV, $2p_{3/2}$) while Ag 3d show only peaks due to elemental Ag (368.2 eV ($3d_{5/2}$) and 374.2 eV ($3d_{3/2}$)), which confirms chemical reduction. The C 1s spectra indicate the presence of C–P (287.4 eV) and C–OH (285.9 eV) from THPC along with the other C 1s peaks observed for MMO. In both MMO and MMO–Ag, the O 1s spectra exhibit peaks due to lattice metal-oxygen linkage (530.2 eV), hydroxyl groups (532 eV), *etc.* The detailed analysis and Fig. S6–S8 are provided in ESI.†

The specific surface area of the spiky MMO and MMO–Ag, and their adsorption isotherms obtained from BET analysis are shown in Fig. S9 (ESI†). MMO shows type II isotherm and MMO–Ag exhibits type IV isotherm with a hysteresis loop.[53] The MMO has a specific surface area of 103 $m^2 g^{-1}$ and the high surface area of the MMO is attributed to its spiky morphology. The surface area decreases to 73.5 $m^2 g^{-1}$ after decoration with CuO and silver nanoparticles (MMO–Ag). The synthesized MMO and MMO–Ag have a higher surface area than the usual metal oxide morphology.[54]

The UV-vis spectra of MMO and MMO–Ag are shown in Fig. 6(a) and (b) and the optical band gap calculation in Fig. 6(c) and (d). MMO shows only absorption in the UV region corresponding to the band edge of (Zn, Ti, Si) O. The absorption spectra of MMO–Ag clearly indicate a higher absorption in the vis-NIR region than MMO and show a broad absorption tail extending towards the NIR region. The presence of CuO and Ag nanoparticles are responsible for increased absorption in the visible region. The absorption peak due to surface plasmons of Ag nanoparticles is observed at 413 nm.[55,56] The presence of intermediate surface states, which might arise because of oxygen-deficient species, can also contribute to the extended absorption tail in the visible region.[57] This oxygen-deficient species can also enhance the antimicrobial properties.[58] The optical bandgap of the MMO is found to be 3.28 eV since the

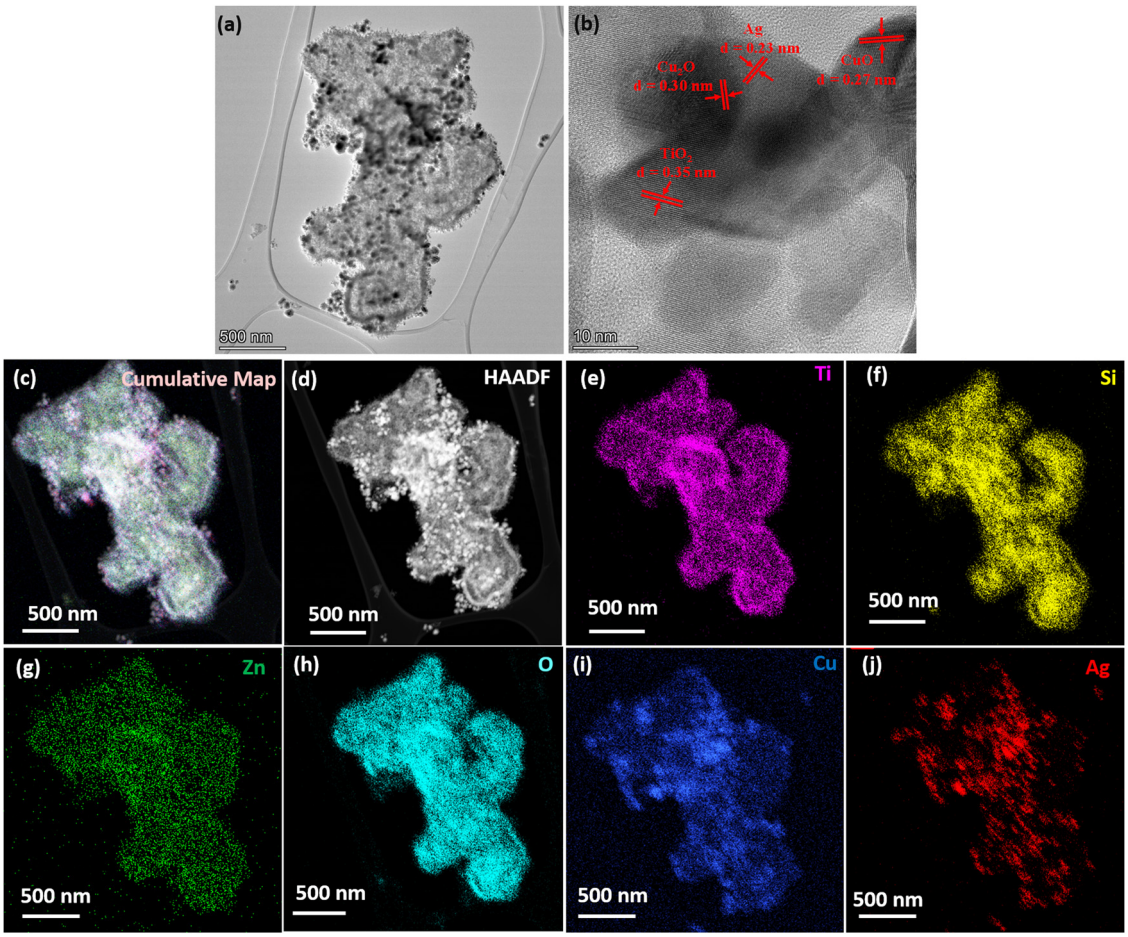

Fig. 4 (a) TEM image of spiky MMO–Ag. (b) HRTEM analysis of MMO–Ag. (c)–(j) TEM-EDS mapping of MMO–Ag. (c) EDS composite map of Ti, K (magenta), Si K (yellow), Zn K (green), O K (aqua), Cu K (blue) and Ag, L (red), (d) HAADF image, (e) Ti, K, (f) Si, K, (g) Zn, K, (h) O, K, (i) Cu, K, and (j) Ag K.

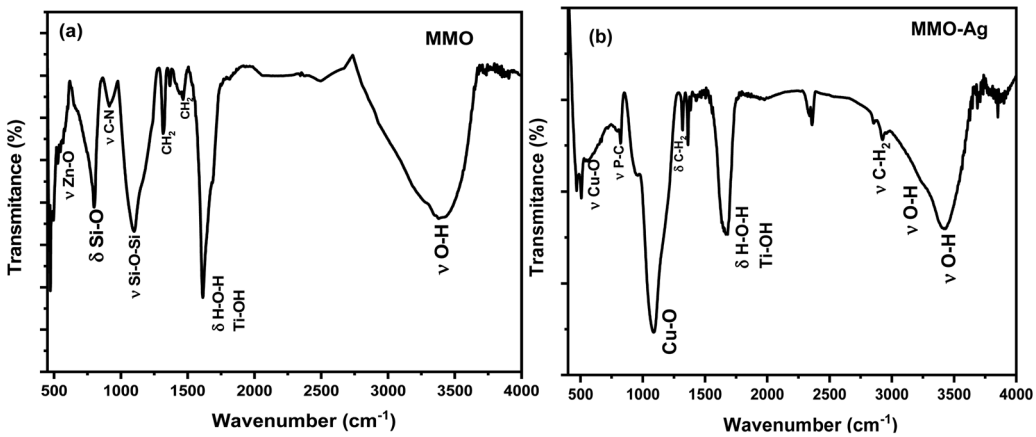

Fig. 5 FTIR spectra of (a) spiky MMO and (b) spiky MMO–Ag.

MMO is rich in titanium oxide, and after the deposition of CuO and Ag, the bandgap is estimated to be 2.58 eV.

The zeta potential of the synthesized MMO–Ag is carried out to estimate the electric charges present on the particles. The particle has a zeta potential of +38.8 mV in 1 mg mL^{-1} of ethanolic solution, which confirms that the particles possess moderate stability.[59] Moreover, it has positive charges, which are imparted due to the positive surfactant. This can be beneficial for elevating the antimicrobial property of the material. A detailed discussion is given in the later section. The average particle size of

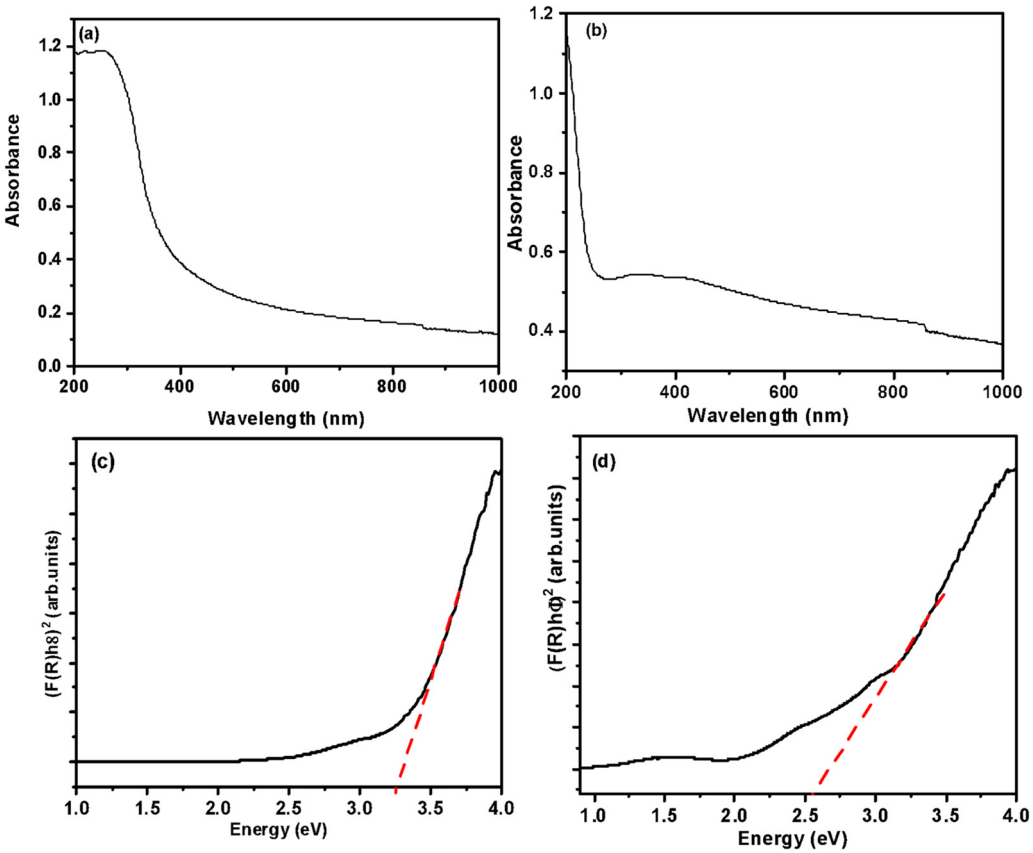

Fig. 6 UV-visible-NIR absorption spectra of (a) spiky MMO and (b) MMO–Ag. Tauc plots of (c) spiky MMO and (d) MMO–Ag.

MMO–Ag from dynamic light scattering is 1.2 μm, which agrees with the microscopy results (Fig. S10, ESI†). The poly dispersion index is estimated to be 0.46.

Antimicrobial studies

To investigate the antibacterial action, the zone of inhibition (ZI) exhibited by the MMO–Ag nanoformulation against *E. coli* and *S. aureus* is evaluated employing the agar well diffusion method. A larger diameter of the ZI shows the effectiveness of the antimicrobial material in inhibiting bacterial growth. In order to understand the effect of the spiky corona of MMO–Ag, spherical MMO–Ag without spikes is but having a similar composition is also tested for antibacaterial activity.

From Fig. 7, a clear ZI is seen around all the wells, which confirms that both spiky and spherical nanoformulations are able to inhibit the growth of *E. coli* and *S. aureus* at different concentrations. The numbers 1, 2, and 3 in the photographs correspond to the loadings of 2.5, 5 and 10 mg mL^{-1} of the synthesized material on the test bacteria, respectively and number 4 corresponds to the standard antibiotic ciprofloxacin. The corresponding inhibition zone values are shown in the bar graph (Fig. 7(c) and (f)). It is clear from the results that spiky MMO–Ag shows enhanced antibacterial properties though the chemical composition is similar in both cases. This can be attributed to the spiky morphology possessing sharp nanometric tips that may physically puncture the cell membrane of the pathogens providing additional antimicrobial effect.

The nanoformulation shows a superior effect on *S. aureus* at a lower concentration of the nanoformulation, as we observe from the bar diagram. Even 2.5 mg mL^{-1} of the spiky nanoformulation shows 14 mm ZI, indicating that even a lower concentration of nanoformulation is enough to induce antimicrobial activity against *S. aureus*. In the case of *E. coli*, ZI is just 11 mm for 2.5 mg mL^{-1}, though it has improved with a higher concentration of formulation. The better results observed in the Gram-positive *S. aureus* may be either due to its geometry, cell wall thickness, or charges on the cell membrane. The cell wall thickness of *E. coli* (4 nm) is much lesser than that of *S. aureus* (20–40 nm); however, the zeta potential of *S. aureus* (−37.1 mV) is much greater than that of *E. coli* (−4.9 mV to −49 mV).[60] MMO–Ag also shows good antibacterial activity against *B. cereus.* The photographs of ZI of MMO–Ag against *B. cereus* and bar diagrams showing ZI for various concentrations of MMO–Ag are shown in Fig. S11(a) and (b) (ESI†). It can be noticed that for 5 mg mL^{-1} of the MMO–Ag concentration, ZI is 10 mm, and as the concentration is increased to 10 mg mL^{-1}, ZI also increased to 15 mm. Control experiments are also performed with MMO without Ag deposition (spiky MMO–CuO) to monitor the antibacterial activity in the absence of Ag and they still exhibit good activity

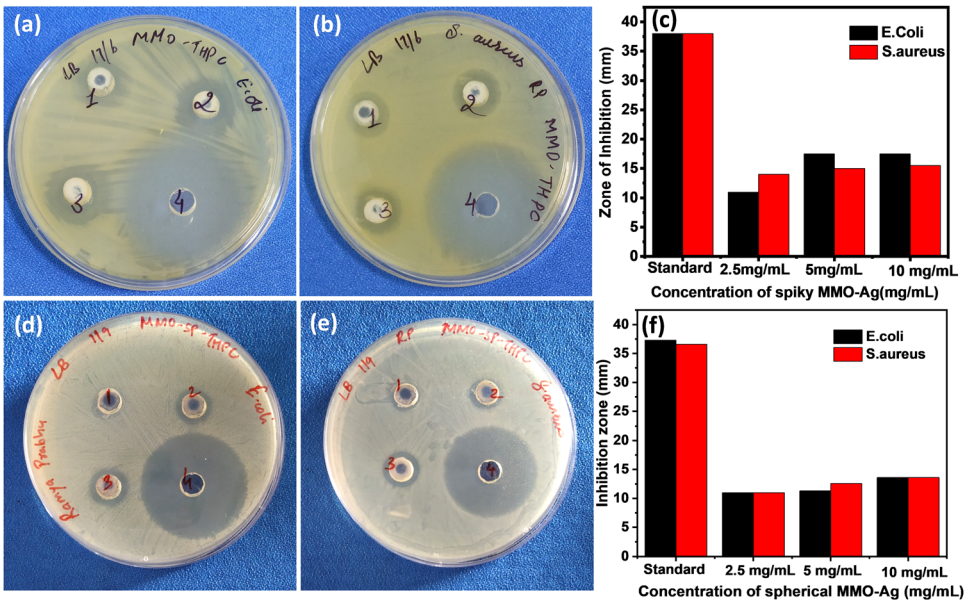

Fig. 7 Photographs of ZI: (a) spiky MMO–Ag against *E. coli*, (b) spiky MMO–Ag against *S. aureus*, (d) spherical MMO–Ag against *E. coli* and (e) spherical MMO–Ag against *S. aureus*. Bar diagrams showing ZI for various concentrations of (c) Spiky MMO–Ag and (f) Spherical MMO–Ag.

against *E. coli* and *S. aureus* with the observed ZI close to 10 mm, slightly lower than that of MMO–Ag (Fig. S12, ESI†).

To further establish the antimicrobial property of MMO–Ag, the plate count method is carried out. The results of the plate count method are shown in Fig. S13 (ESI†) for *E. coli* and Fig. S14 (ESI†) for *S. aureus*, respectively. In this method, we have checked the susceptibility of *E. coli* and *S. aureus* bacteria against MMO–Ag. Even a single colony of the bacteria is not seen to grow in the LB agar plate (Fig. S13(d)–(f), ESI† for *E. coli* and Fig. S14(d)–(f), ESI† for *S. aureus*). When the control experiment is performed without the nanoformulation, well-grown bacterial colonies are observed in Fig. S13(a)–(c), ESI† for *E. coli* and Fig. S14 (a)–(c) (ESI†) for *S. aureus*. If the bacteria were alive, they could have grown into colonies in the case of MMO–Ag-treated bacterial solutions. These results indicate that the above-mentioned microorganisms are highly susceptible to MMO–Ag. However, spherical MMO–Ag shows less antibacterial properties against *S. aureus* and a few colonies are observed to have grown in 10^{-4} CFU mL^{-1} concentrations of the bacteria (Fig. S15, ESI†).

It is observed from the experiments that spiky MMO shows better performance than spherical MMO. The foremost reason for this is the very high surface area-to-volume ratio of the spiky structure in comparison to the sphere. This results in strong interaction with the bacteria. When exerting antimicrobial activity,[61] the nanoparticles first interact with the bacterial cell membrane to form pores or puncture the structure at several places *via* cell fluidization. This modifies the hydrophobicity of the cell membrane. If the nanoparticle is very small (of the order of a few nanometers) in size, they also enter the cell and react with the cytosol and other cell components. However, larger particles cannot enter into the cell, but once the pores on the bacterial cell walls are formed, the cytoplasmic content diffuses out of the pores formed. They also destabilize the proteins and enzymes causing impairment in their metabolism. This leads to structural collapse, and ultimately cell death. Physical puncturing is possible when the bacteria come into contact with the MMO particles. However, the ZI is of the order of millimetres and it is imperative that other forces come into play. In general, the electrostatic, hydrophobic, hydrogen-bonding and van der Waals interactions are involved in all these processes.

To understand the effect of geometry and electrostatic nature of the antimicrobial activity, we estimated the interaction energy between the spiky MMO and the bacteria using the Derjaguin–Landau–Verwey–Overbeek (DLVO) theory. The DLVO theory has been applied to regular geometries such as smooth sphere, cylinders, and plates under Derjaguin's (DA) approximation.[34,37,38] For the spiky geometry, the surface element integration (SEI) technique is used to calculate the interaction energy. The details of the SEI theory for estimating the DLVO interaction energy between a spiky sphere and a smooth sphere are explained earlier. To validate the derivation for spiky MMO, the results obtained for two smooth spheres using the SEI technique (Fig. 8(b) and (c)) are compared with DA approximation (Fig. 8(a)). It is observed that the results derived from both techniques are in a comparable range. Moreover, it has been reported in the literature that the SEI technique predicts the results better than the DA technique.[34,37,38] All the results for the SEI technique are compiled by dividing the surface into 400 elements. By increasing the number of elements, the pattern of the results did not change except for the numerical singularity when the particles are very close to each other. Fig. 8(d)–(i) are compiled for interactions between spiky MMO and both kinds of bacteria by varying the

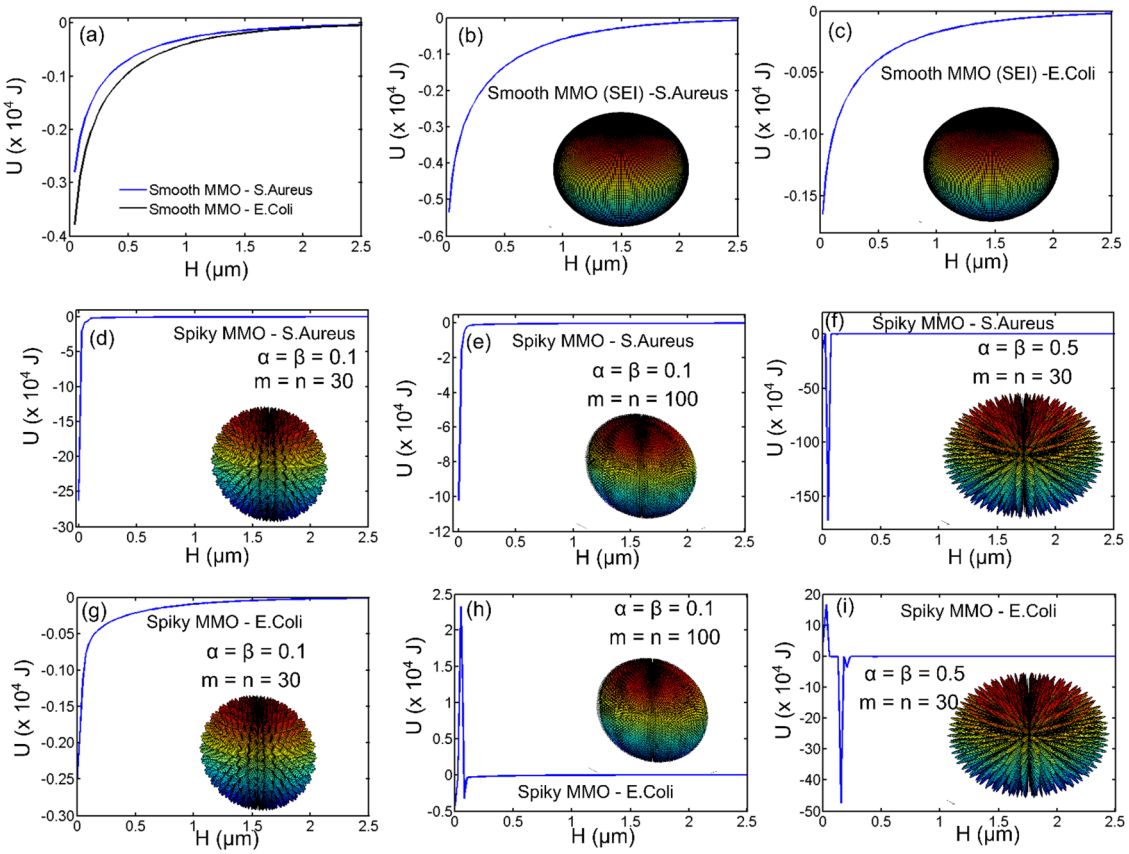

Fig. 8 DLVO interaction energy between MMO and bacteria (*S. aureus* and *E. coli*) using (a) DA approximation and (b)–(i) SEI technique. (a)–(c) are for smooth spheres and (d)–(i) are obtained for spiky MMO with different densities of spikes (*m*, *n*) and spike aspect ratios (*α*, *β*).

density and aspect ratio of the spikes. It is observed that there is a strong net attractive interaction between MMO particles and both kinds of bacteria. The attraction increases by the order of 10^2 for spiky particles when compared to smooth spheres. For the MMO with a given aspect ratio (*α*, *β*) (Fig. 8(d) and (e)), the interaction energy varies with the spike density (*m*, *n*) and can be optimized for a certain density. As the spikes' aspect ratio increases (that is, for higher (*α*, *β*), wherein they become more pointed, the net attraction increases significantly for both types of bacteria (Fig. 8(f) and (i)). The attractive interaction between the spiky MMO and *S. aureus* (Fig. 8(a), (b) and (d)–(f)) is much greater than that between the spiky MMO and *E. coli* (Fig. 8(a), (c) and (g)–(i)). Moreover, for spiky MMO with a certain density and spike aspect ratio (Fig. 8(h) and (i)), there is a very high activation barrier that lowers the interaction between the spiky MMO and *E. coli.* Hence, the spiky MMO shows a superior antimicrobial effect on *S. aureus* bacteria in comparison to *E. coli.*

Further, the MIC of the nanoformulation against *S. aureus* bacteria is found by a microdilution assay. The photographs of 96-well plates containing a *S. aureus* solution treated with different concentrations of MMO–Ag are shown in Fig. S16 (ESI†). The untreated well (represented as UT) shows that bacteria are well grown in the media. The plot of cell viability *vs.* concentration of MMO–Ag is shown in Fig. 9. The graph clearly shows that bacterial cell viability decreases drastically as the concentration of nanoformulation increases from 100 μg mL^{-1} to 200 μg mL^{-1}; however, as the concentration of the nanoformulation increases further, there is no significant decrease in bacterial cell viability. The calculated MIC_{50} value is 107.2 μg mL^{-1}. The MBC of MMO–Ag to reduce 99.9% of the initial concentration of *S. aureus* bacteria is tested by the agar plate method. The photographs reveal that the bacterial lawn is well grown in the untreated portion of the agar plate (Fig. S17(a), ESI†) while the growth of the bacteria is completely prohibited in 20 mg mL^{-1} concentration of MMO–Ag (Fig. S17(b), ESI†). Even at 2.5 mg mL^{-1} concentration, the viability of the bacteria is not detected. A few bacterial colonies can be observed in the 1.25 mg mL^{-1} concentration of MMO–Ag (Fig. S17(f), ESI†). These results clearly show that the MBC of the MMO–Ag is 2.5 mg mL^{-1}, as shown in Fig. S17(e) (ESI†). A comparison of the present study with the reported MIC or equivalent values for various metal oxide composites in the literature is presented in Table S1 (ESI†). A MIC of 0.1 mg mL^{-1} obtained in the case of spiky MMO–Ag is excellent compared to the reported ones.

We have further explored the antimicrobial properties of the synthesized spiky MMO–Ag on the melt-blown fabric applied as a coating. MMO–Ag dispersion is coated onto melt-blown fabrics used for mask fabrication by the dip-coating method.

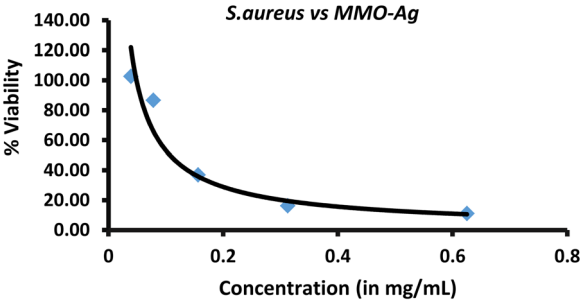

Fig. 9 Percentage viability of *S. aureus vs.* concentration of spiky MMO–Ag.

The cleaned melt-blown fabric is immersed in dispersions of 5 mg mL^{-1} of the MMO–Ag for 1 h followed by drying at 80 °C for one hour. The FESEM images of the coated melt-blown fabric are shown in Fig. 10(a) and (b). From the FESEM images, it is clear that the spiky structures have encapsulated all the fabric strands without blocking the pores of the fabric. The spiky MMO–Ag-coated melt-blown fabric was tested for activity against bacteria using the agar plate method (Fig. 10(c) and (d)). The excellent ZI shows that the coated fabric is effective to deactivate bacteria, *E. coli*, and *S. aureus*. The ZI values are summarized in Table S2 (ESI†). The above-mentioned results further support that the material has excellent antibacterial properties against both Gram-negative and Gram-positive bacteria and the utility of these formulations for coating fabrics and surfaces.

The antiviral property of spiky MMO–Ag is tested employing nonwoven fabric swatches coated with the nanoformulation in contact with the MS2 bacteriophage virus as the test organism for 2 hours and 24 hours at 35 °C, and the results are tabulated in Table S3 (ESI†). The results show that the nanoformulation-coated melt-blown fabric is virucidal against the bacteriophage virus. Within 2 h of contact, the log reduction of the virus achieved is 2.11 corresponding to a 99.21% reduction of the virus. After 24 h of contact, the percentage reduction is noted to be 94.36%. The control experiments conducted under similar conditions employing uncoated fabrics do not show any reduction in the virus concentration, indicating that the non-woven plain melt-blown fabric does not possess any inherent virucidal property. The experiment indicates that the developed spiky MMO–Ag possesses excellent antiviral property in addition to antibacterial property. The results of the cytotoxicity of MMO–Ag on VeroE6 cells after 24 h and 48 h indicate that MMO–Ag is not cytotoxic at 1 mg mL^{-1} and 0.5 mg mL^{-1} (Fig. S18(a) and (b), ESI†).

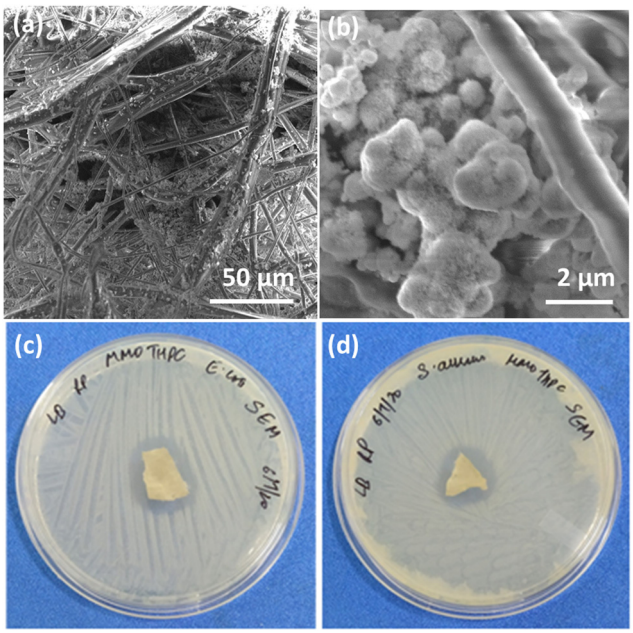

Fig. 10 FESEM images of MMO–Ag coated on the meltblown fabric (a) low magnification and (b) high magnification. Photographs of the MMO–Ag-coated meltblown fabric showing the ZI against (c) *E. coli* and (d) *S. aureus*.

Reusability and self-cleaning property of the nanoformulation-coated fabric

There are several methods for reusing the N95 mask, and its filtering efficiency will vary depending on the decontamination treatments.[62] In the present work, heat, sunlight, and UV irradiation were used to test the reusability of fabrics coated with the antimicrobial MMO–Ag. The bacteria-treated mask fabrics were heated in an oven for 30 min or exposed to natural sunlight for 3 hours, or irradiated with UV light at 365 nm for 30 minutes. The agar plate method was used to test the antimicrobial properties after the reusability treatment. Fig. 11 shows the photographs of inhibition zones of the reused melt-blown fabric coated with MMO–Ag after subjecting to the above-mentioned treatments. These procedures are non-destructive, and the nanoformulation retains its properties even after being subjected to them. The excellent inhibition zones for *S. aureus* growth demonstrate that the bactericidal properties of the material are preserved. Table S4 (ESI†) shows the area of the ZI after three treatments and supports the reusability claim.

MMO–Ag comprising photocatalytic metal oxides and, silver facilitates the degradation of organic matter, and the presence of Ag is known to enhance the photodegradation.[63] We exploited this property of the material and studied the degradation of *E. coli* bacteria on MMO–Ag by FESEM imaging. It is clearly observed that the cylindrical shape of *E. coli* is intact on silicon (Fig. 12(a)) before UV illumination. However, after UV illumination, aggregated bacterial cells are seen on a silicon substrate, indicating deactivation upon UV exposure but their cylindrical shapes are visible without any major disruption in their morphology (Fig. 12(c)). In the case of MMO–Ag, the bacteria are seen completely covering the material, as shown in Fig. 12(b). Interestingly, it can be noticed that the structure of the bacteria is mostly collapsed even before UV illumination, indicating the superior antibacterial nature of MMO–Ag. Most importantly, after UV exposure, the spiky

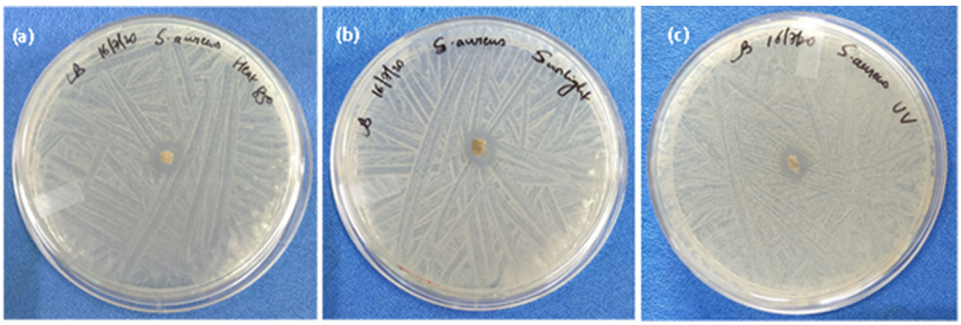

Fig. 11 Reusability: photographs showing the inhibition zone of the reused meltblown fabric coated with MMO–Ag after (a) heating in an oven at 85 °C, (b) exposure to sunlight and (c) UV illumination.

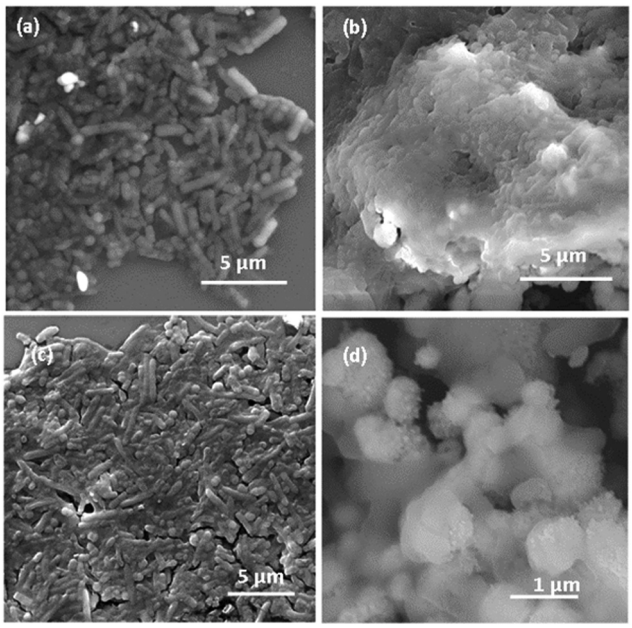

Fig. 12 FESEM images of *E. coli* bacteria on (a) bare Si before UV illumination, (b) MMO–Ag before UV illumination, (c) Si substrate after UV illumination and (d) MMO–Ag after UV illumination.

nature of the nanoformulation is visible due to the degradation of bacteria, hence exposing the fresh surface of MMO–Ag for further use (Fig. 12(d)). The photo-induced cleaning effect can be considered responsible in the case of MMO–Ag for the photodegradation of bacteria. When the above-mentioned substrates are irradiated by the UV light, reactive oxygen species (ROS) are produced, which causes severe damage to the cell membrane of *E. coli* (Fig. 12(c)).

The UV illumination causes degradation of the bacterial matter apart from the deactivation effect. As the pathogen comes into contact with MMO–Ag due to its physical and chemical effects, it is killed, which is evident from the plate count method. Further, when MMO is combined with Ag (MMO–Ag), the photocatalytic degradation property of the metal oxide is enhanced due to improved charge separation, and can completely degrade the microbe or any organic matter (like sweat), regenerating a fresh surface of spiky MMO, and hence, clean fabric for further use.

The UV illumination of MMO results in a non-uniform distribution of electric field due to the MMO geometry with a very strong field near the spikes, and is explained using a computational model by computing the electric field distribution for a single spike with and without an Ag particle. The electric field distribution is calculated by solving the electromagnetic wave equation, under the assumption of no external charges and current. This is given as follows:

$$\nabla^2 E - c^2 \frac{\partial^2}{\partial t^2} E = 0 \qquad (10)$$

where c is the velocity of light. We have used the 2D model on the xy-plane to understand the mechanism. A single spike with the dimensions taken from the experimental results is assumed to be on a MMO substrate surrounded by air with and without Ag nanoparticles on its tip. The incident UV wave is assumed to travel perpendicular to the surface along the negative z-axis and the electric field is polarized along the x-axis. We have applied the Floquet periodicity along the x-axis. The refractive index of glass is 1.5. The refractive index for MMO is taken as the average of the constituent metal oxides (from the COSMOL library) and that of Ag from the literature.[64] From Fig. 13(a) and (b), it is observed that the electric field enhancement due to the spiky geometry is higher than the critical field for the electrical lysis of bacteria, which is about 1–2 kV cm^{-1}. Additionally, when Ag nanoparticles are present on the tip, the field enhancement is nearly 2 times when compared to spikes without Ag nanoparticles.

The antimicrobial mechanism of the MMO–Ag is mainly attributed to the mechano-bactericidal effect due to spiky morphology, generation of reactive oxygen species (ROS) and electrostatic attraction between the nanoformulation and pathogens. There are few reports on the antimicrobial effect of the nanoformulation due to its physical properties. It is reported that shape, size, surface charges, solubility, and agglomeration of the nanoparticles play an important role in the antimicrobial property.[23] The metal and metal oxide with a different morphology show superior antimicrobial properties to the spherical counterpart.[65,66] Due to the spiky topography of the synthesized nanoformulation, it imparts mechano-

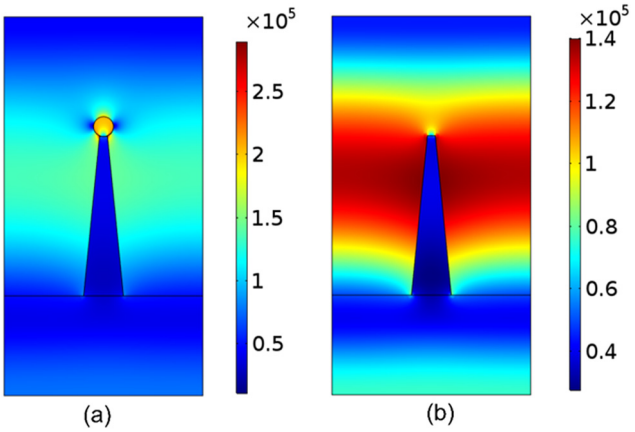

Fig. 13 Simulation results for the magnitude of electric field distribution around a single spike (a) with an Ag nanoparticle and (b) without any Ag nanoparticle.

bactericidal effects to the cell membrane. The nanoprotrusions present on the material endow the microbial cell membrane with mechanical forces, which further stretch the membrane beyond its elastic limit. This substantial stretching leads to the rupture of the cell, ultimately causing cell lysis. Physical piercing of the cell wall is also possible due to the sharp projections of the synthesized material, which also leads to cell death.[67]

The cationic surfactants are the most well-known class of antimicrobial agents. Due to their positive zeta potential, they show greater affinity towards the bacterial cell wall by electrostatic interaction, as the cell membrane of the pathogens is negatively charged and easily interacts with the positive sites of the cationic surfactant. Strongly adhered nanoformulations disrupt the cell wall and dissolve the lipid layer of microbes.[68] A patented research work by K. I. Ajoku *et al.* has shown that the antimicrobial properties of composites of peroxyacetic acid and phosphonium compounds such as THPC are more effective than those of the individual component. The prepared composition is effective against bacteria, yeasts, moulds and algae.[69] The cationic moieties $[P(CH_2OH)_4]^+$ present in the surfactant endow superior antimicrobial properties to the material. All these novel physicochemical properties impart high antimicrobial properties to the synthesized MMO–Ag nanoformulation. The chemical effect also arises from silver nanoparticles and mixed metal oxide structures. Ag nanoparticles can bind to the sulphur functional group of the bacterial cell membrane and further interact with the proteins present in the interior of the cell, finally causing bacterial death.[70–72] Q. L. Feng *et al.* have observed that silver nanoparticles interact with the proteins present in the cell's interior and also the phosphorous present in the DNA of the bacteria.[72] This will affect cell division and finally cause bacterial death.

MMOs containing TiO_2, ZnO, and CuO are photoactive materials generating charge carriers when they get excited by the UV and visible light irradiation.[73,74] Moreover, the surface plasmon properties of silver nanoparticles can extend the light response to the visible absorption range and also aid in charge separation.[75] The antimicrobial effect of metal oxide nanoparticles is attributed to the generation of ROS, release of ions, and electrostatic interaction with the cell membrane.[76] Once the metal oxide attaches to the cell membrane, pitting occurs due to ROS formation, which greatly damages the cell wall.[77] It is reported that the TiO_2 thin film photocatalyst effectively kills *E. coli* by UV exposure; however, the endotoxin from the cell wall is also degraded.[78] The decomposition of the cell wall and cell membrane by Ag/AgBr/TiO_2 during visible light illumination is shown by the leakage of K^+ ions from the interior of the bacteria.[79] The photocatalysis properties of montmorillonite-supported Ag/TiO_2 nanoparticles are reported to be responsible for the degradation of *E. coli* bacteria rather than poisoning from the silver.[80] The electrons and holes are separated and the photogenerated electron combines with the oxygen present on the surface of the MMO generating $^{\bullet}O_2^-$ radicals. The generated holes will react with water and produce $^{\bullet}OH$ radicals. In the final step, $^{\bullet}OH$, $^{\bullet}O_2^-$, and h^+ react with the pathogen and lead to the degradation of products.[81–83] The schematic of the plausible antimicrobial mechanism of MMO–Ag is shown in Fig. S19 (ESI†) along with the possible reactions that occur upon irradiation of light.

A prototype of the nanoformulation-coated antimicrobial face mask with N-95 configuration was fabricated, and is shown in Fig. S20 (ESI†). The top and bottom views of the fabricated mask are shown in Fig. S20 (a) and (b) (ESI†) and the antimicrobial nanoformulation in Fig. S20(c) (ESI†). The bacterial filtration efficiency (BFE) of the designed nanoformulation-coated face mask was tested using a biological aerosol of *S. aureus* by ASTM: F 2101-19 (Table S5, ESI†). The mask sample coated with the nanoformulation exhibited 99.35% BFE when analyzed as per the ASTM: F 2101-19 standard. A good particle filtration efficiency of 99.67% was reported for the developed mask towards particles of size 0.3 micron(Table S6, ESI†).

Conclusions

A novel nanoformulation consisting of the mixed metal oxides of TiO_2, ZnO, SiO_2, and CuO with silver nanoparticles capped with a cationic surfactant is demonstrated for antimicrobial coatings. The antimicrobial property of the prepared dispersion was verified using agar well diffusion, agar plate, plate count, and microdilution methods. The enhanced zone of inhibition values revealed that the unique spiky morphology induced superior antimicrobial activities against Gram-positive and Gram-negative bacteria as well as bacteriophage viruses. The sharp nanospiky corona of the material induced a mechano-bactericidal effect. The electrostatic attraction between the cationic surfactant and the pathogen's cell wall can lead to the disruption of the cell wall, resulting in cell death. This is further enhanced by the ROS generation due to the photoactive metal oxide present in the nanoformulation. The calculated energy profiles between the spiky MMO and bacteria derived from DLVO theory indicated that the presence of the spiky topology increased the interaction energy by 10^2 in comparison

with their smooth counterpart. Furthermore, for certain spike densities and aspect ratios, there is a high activation barrier between the spiky MMO and *E. coli* bacteria. This explains the lower antimicrobial activity on *E. coli* in comparison to *S. aureus*. The nanoformulation-coated mask fabric is demonstrated to be reusable and capable of self-cleaning as the photoactive material present in the nanoformulation successfully degrades the bacteria and organic matter upon UV irradiation regenerating the fresh surface for further use. The self-cleaning property of spiky MMO can be attributed to enhanced electric field intensity near the tips, which further increases by a factor of 2 in the presence of silver nanospheres. An antimicrobial face mask was designed, which showed excellent BFE and particle filtration efficiency.

Conflicts of interest

The authors declare no conflict of interest.

Acknowledgements

The authors acknowledge the Central Research Facilities, CeNS, for characterization facilities. RPB acknowledges financial support from DST-inspire fellowship (IF160653). RPB acknowledges Siddharth Dubey, Ashutosh Acharya, and Pearl Gulati for useful discussions. All the antibacterial studies are done at Cell Kraft Biotech Pvt. Ltd., and Dextrose Technologies Pvt. Ltd., Bengaluru. Bacterial filtration efficiency test and antiviral test against MS2 bacteriophage were carried out at Biotech Testing Services Mumbai, India. The particle filtration efficiency was done at the South India Textile Research Association (SITRA), Coimbatore Tamil Nadu, India. Cytotoxicity assay was done at RCB, New Delhi.

References

1 P. Prasher and M. Sharma, *Nanomedicine*, 2021, **16**, 1183–1186.
2 C. Weiss, M. Carriere, L. Fusco, L. Fusco, I. Capua, J. A. Regla-Nava, M. Pasquali, M. Pasquali, M. Pasquali, J. A. Scott, F. Vitale, F. Vitale, M. A. Unal, C. Mattevi, D. Bedognetti, A. Merkoçi, A. Merkoçi, E. Tasciotti, E. Tasciotti, A. Yilmazer, A. Yilmazer, Y. Gogotsi, F. Stellacci and L. G. Delogu, *ACS Nano*, 2020, **14**, 6383–6406.
3 C. J. Neal, C. R. Fox, T. S. Sakthivel, U. Kumar, Y. Fu, C. Drake, G. D. Parks and S. Seal, *ACS Nano*, 2021, **15**, 14544–14556.
4 P. Y. Chia, K. K. Coleman, Y. K. Tan, S. W. X. Ong, M. Gum, S. K. Lau, X. F. Lim, A. S. Lim, S. Sutjipto, P. H. Lee, T. T. Son, B. E. Young, D. K. Milton, G. C. Gray, S. Schuster, T. Barkham, P. P. De, S. Vasoo, M. Chan, B. S. P. Ang, B. H. Tan, Y. S. Leo, O. T. Ng, M. S. Y. Wong, K. Marimuthu, D. C. Lye, P. L. Lim, C. C. Lee, L. M. Ling, L. Lee, T. H. Lee, C. S. Wong, S. Sadarangani, R. J. Lin, D. H. L. Ng, M. Sadasiv, T. W. Yeo, C. Y. Choy, G. S. E. Tan, F. Dimatatac, I. F. Santos, C. J. Go, Y. K. Chan, J. Y. Tay, J. Y. L. Tan, N. Pandit, B. C. H. Ho, S. Mendis, Y. Y. C. Chen, M. Y. Abdad and D. Moses, *Nat. Commun.*, 2020, **11**, 2800.
5 J. L. Santarpia, D. N. Rivera, V. L. Herrera, M. J. Morwitzer, H. M. Creager, G. W. Santarpia, K. K. Crown, D. M. Brett-Major, E. R. Schnaubelt, M. J. Broadhurst, J. V. Lawler, S. P. Reid and J. J. Lowe, *Sci. Rep.*, 2020, **10**, 12732.
6 R. R. Naik and S. Singamaneni, *Chem. Rev.*, 2017, **117**, 12581–12583.
7 E. Lurie-Luke, *Biotechnol. Adv.*, 2014, **32**, 1494–1505.
8 L. R. Volpatti, R. P. Wallace, S. Cao, M. M. Raczy, R. Wang, L. T. Gray, A. T. Alpar, P. S. Briquez, N. Mitrousis, T. M. Marchell, M. S. Sasso, M. Nguyen, A. Mansurov, E. Budina, A. Solanki, E. A. Watkins, M. R. Schnorenberg, A. C. Tremain, J. W. Reda, V. Nicolaescu, K. Furlong, S. Dvorkin, S. S. Yu, B. Manicassamy, J. L. Labelle, M. V. Tirrell, G. Randall, M. Kwissa, M. A. Swartz and J. A. Hubbell, *ACS Cent. Sci.*, 2021, **7**, 1368–1380.
9 P. M. Chen, W. Y. Pan, P. K. Luo, H. N. Phung, Y. M. Liu, M. C. Chiang, W. A. Chang, T. L. Tien, C. Y. Huang, W. W. Wu, W. T. Chia and H. W. Sung, *ACS Nano*, 2021, **15**, 7596–7607.
10 H. J. Chen, T. Hang, C. Yang, D. Liu, C. Su, S. Xiao, C. Liu, D. A. Lin, T. Zhang, Q. Jin, J. Tao, M. X. Wu, J. Wang and X. Xie, *ACS Cent. Sci.*, 2019, **5**, 960–969.
11 C. Nie, M. Stadtmüller, H. Yang, Y. Xia, T. Wolff, C. Cheng and R. Haag, *Nano Lett.*, 2020, **20**, 5367–5375.
12 L. Huang, X. Mao, J. Li, Q. Li, J. Shen, M. Liu, C. Fan and Y. Tian, *ACS Nano*, 2023, **17**, 9155–9166.
13 N. Wang, A. R. Ferhan, B. K. Yoon, J. A. Jackman, N. J. Cho and T. Majima, *Chem. Soc. Rev.*, 2021, **50**, 9741–9765.
14 S. M. Imani, L. Ladouceur, T. Marshall, R. Maclachlan, L. Soleymani and T. F. Didar, *ACS Nano*, 2020, **14**, 12341–12369.
15 Á. Serrano-Aroca, K. Takayama, A. Tuñón-Molina, M. Seyran, S. S. Hassan, P. Pal Choudhury, V. N. Uversky, K. Lundstrom, P. Adadi, G. Palù, A. A. A. Aljabali, G. Chauhan, R. Kandimalla, M. M. Tambuwala, A. Lal, T. M. Abd El-Aziz, S. Sherchan, D. Barh, E. M. Redwan, N. G. Bazan, Y. K. Mishra, B. D. Uhal and A. Brufsky, *ACS Nano*, 2021, **15**, 8069–8086.
16 H. Li, J. Zhang, L. Yang, H. Cao, Z. Yang, P. Yang, W. Zhang, Y. Li, X. Chen and Z. Gu, *Adv. Funct. Mater.*, 2023, **33**, 2212193.
17 S. Kumar, M. Karmacharya, S. R. Joshi, O. Gulenko, J. Park, G. H. Kim and Y. K. Cho, *Nano Lett.*, 2021, **21**, 337–343.
18 C. C. Coelho, T. Padrão, L. Costa, M. T. Pinto, P. C. Costa, V. F. Domingues, P. A. Quadros, F. J. Monteiro and S. R. Sousa, *Sci. Rep.*, 2020, **10**, 19098.
19 A. Aditya, S. Chattopadhyay, D. Jha, H. K. Gautam, S. Maiti and M. Ganguli, *ACS Appl. Mater. Interfaces*, 2018, **10**, 15401–15411.
20 X. Qiu, M. Miyauchi, K. Sunada, M. Minoshima, M. Liu, Y. Lu, D. Li, Y. Shimodaira, Y. Hosogi, Y. Kuroda and K. Hashimoto, *ACS Nano*, 2012, **6**, 1609–1618.
21 G. He, M. Wan, Z. Wang, X. Zhou, Y. Zhao and L. Sun, *Prog. Org. Coat.*, 2023, **182**, 107664.

22 G. Ren, J. S. Oxford, P. W. Reip, R. Lambkin-Williams and A. Mann, *US. Pat.*, US20100040655A1, 2007.
23 K. Gold, B. Slay, M. Knackstedt and A. K. Gaharwar, *Adv. Thermoelectr.*, 2018, **1**, 1700033.
24 A. Raghunath and E. Perumal, *Int. J. Antimicrob. Agents*, 2017, **49**, 137–152.
25 A. Abbaszadegan, Y. Ghahramani, A. Gholami, B. Hemmateenejad, S. Dorostkar, M. Nabavizadeh and H. Sharghi, *J. Nanomater.*, 2015, 720654.
26 L. Zhao, T. Liu, X. Li, Q. Cui, Q. Wu, X. Wang, K. Song and D. Ge, *ACS Biomater. Sci. Eng.*, 2021, **7**, 2268–2278.
27 D. P. Linklater, M. De Volder, V. A. Baulin, M. Werner, S. Jessl, M. Golozar, L. Maggini, S. Rubanov, E. Hanssen, S. Juodkazis and E. P. Ivanova, *ACS Nano*, 2018, **12**, 6657–6667.
28 D. P. Linklater, V. A. Baulin, S. Juodkazis, R. J. Crawford, P. Stoodley and E. P. Ivanova, *Nat. Rev. Microbiol.*, 2021, **19**, 8–22.
29 D. H. K. Nguyen, C. Loebbe, D. P. Linklater, X. Xu, N. Vrancken, T. Katkus, S. Juodkazis, S. Maclaughlin, V. Baulin, R. J. Crawford and E. P. Ivanova, *Nanoscale*, 2019, **11**, 16455–16462.
30 A. S. Joshi, P. Singh and I. Mijakovic, *Int. J. Mol. Sci.*, 2020, **21**, 7658.
31 W. Pajerski, D. Ochonska, M. Brzychczy-Wloch, P. Indyka, M. Jarosz, M. Golda-Cepa, Z. Sojka and A. Kotarba, *J. Nanopart. Res.*, 2019, **21**, 186.
32 A. Roy and K. Chatterjee, *Nanoscale*, 2021, **13**, 647–658.
33 E. Thormann, *Curr. Opin. Colloid Interface Sci.*, 2017, **27**, 18–24.
34 S. Bhattacharjee, C. H. Ko and M. Elimelech, *Langmuir*, 1998, **14**, 3365–3375.
35 C. Zhou and Y. Wang, *Curr. Opin. Colloid Interface Sci.*, 2020, **45**, 28–43.
36 N. A. Falk, *J. Surfactants Deterg.*, 2019, **22**, 1119.
37 S. Bhattacharjee, M. Elimelech and M. Borkovec, *Croat. Chem. Acta*, 1998, **71**, 883–903.
38 S. Bhattacharjee and M. Elimelech, *J. Colloid Interface Sci.*, 1997, **193**, 273–285.
39 E. Martines, L. Csaderova, H. Morgan, A. S. G. Curtis and M. O. Riehle, *Colloids Surf., A*, 2008, **318**, 45–52.
40 L. Bergström, *Adv. Colloid Interface Sci.*, 1997, **70**, 125–169.
41 J. Israelachvili, *Intermolecular and surface forces*, Elsevier, USA, 2011.
42 J. K. Oh, Y. Yegin, F. Yang, M. Zhang, J. Li, S. Huang, S. V. Verkhoturov, E. A. Schweikert, K. Perez-Lewis, E. A. Scholar, T. M. Taylor, A. Castillo, L. Cisneros-Zevallos, Y. Min and M. Akbulut, *Sci. Rep.*, 2018, **8**, 17247.
43 D. Janjaroen, F. Ling, G. Monroy, N. Derlon, E. Mogenroth, S. A. Boppart, W. T. Liu and T. H. Nguyen, *Water Res.*, 2013, **47**, 2531.
44 E. Kłodzińska, M. Szumski, K. Hrynkiewicz, E. Dziubakiewicz, M. Jackowski and B. Buszewski, *Electrophoresis*, 2009, **30**, 3086–3091.
45 T. Fuchigami and K. I. Kakimoto, *J. Mater. Res.*, 2017, **32**, 3326–3332.
46 T. Murayama, J. Chen, J. Hirata, K. Matsumoto and W. Ueda, *Catal. Sci. Technol.*, 2014, **4**, 4250–4257.
47 X. Wang, C. Yan, J. Yan, A. Sumboja and P. S. Lee, *Nano Energy*, 2015, **11**, 765–772.
48 Y. Gao, Y. Masuda, Z. Peng, T. Yonezawa and K. Koumoto, *J. Mater. Chem.*, 2003, **13**, 608–613.
49 F. Rubio, J. Rubio and J. L. Oteo, *Spectrosc. Lett.*, 1998, **31**, 199–219.
50 D. Jesuvathy Sornalatha and P. Murugakoothan, *Mater. Lett.*, 2014, **124**, 219–222.
51 P. K. Raul, S. Senapati, A. K. Sahoo, I. M. Umlong, R. R. Devi, A. J. Thakur and V. Veer, *RSC Adv.*, 2014, **4**, 40580–40587.
52 B. Zhao, T. J. Kolibaba, S. Lazar and J. C. Grunlan, *Cellulose*, 2021, **28**, 5855–5866.
53 M. Thommes, K. Kaneko, A. V. Neimark, J. P. Olivier, F. Rodriguez-Reinoso, J. Rouquerol and K. S. W. Sing, *Pure Appl. Chem.*, 2015, **87**, 1051–1069.
54 S. E. Jin and H. E. Jin, *Nanomateials*, 2021, **11**, 263.
55 D. Paramelle, A. Sadovoy, S. Gorelik, P. Free, J. Hobley and D. G. Fernig, *Analyst*, 2014, **139**, 4855–4861.
56 T. Kathiraven, A. Sundaramanickam, N. Shanmugam and T. Balasubramanian, *Appl. Nanosci.*, 2015, **5**, 499–504.
57 R. Prabhu B, K. Bramhaiah, K. K. Singh and N. S. John, *Nanoscale Adv.*, 2019, **1**, 2426–2434.
58 A. Elbourne, S. Cheeseman, P. Wainer, J. Kim, A. E. Medvedev, K. J. Boyce, C. F. McConville, J. Van Embden, R. J. Crawford, J. Chapman, V. K. Truong and E. Della Gaspera, *ACS Appl. Bio Mater.*, 2020, **3**, 2997–3004.
59 G. V. Lowry, R. J. Hill, S. Harper, A. F. Rawle, C. O. Hendren, F. Klaessig, U. Nobbmann, P. Sayre and J. Rumble, *Environ. Sci.: Nano*, 2016, **3**, 953–965.
60 X. Liang, C. Liao, M. L. Thompson, M. L. Soupir, L. R. Jarboe and P. M. Dixon, *Front. Microbiol.*, 2016, **7**, 1732.
61 A. S. Joshi, P. Singh and I. Mijakovic, *Int. J. Mol. Sci.*, 2020, **21**, 1–24.
62 L. Liao, W. Xiao, M. Zhao, X. Yu, H. Wang, Q. Wang, S. Chu and Y. Cui, *ACS Nano*, 2020, **14**, 6348–6356.
63 K. Bramhaiah, V. N. Singh and N. S. John, *Phys. Chem. Chem. Phys.*, 2016, **18**, 1478–1486.
64 P. B. Johnson and R. W. Christy, *Phys. Rev. B: Solid State*, 1972, **6**, 4370.
65 L. M. Gilbertson, E. M. Albalghiti, Z. S. Fishman, F. Perreault, C. Corredor, J. D. Posner, M. Elimelech, L. D. Pfefferle and J. B. Zimmerman, *Environ. Sci. Technol.*, 2016, **50**, 3975–3984.
66 S. Pal, Y. K. Tak and J. M. Song, *Appl. Environ. Microbiol.*, 2007, **73**, 1712–1720.
67 K. Modaresifar, S. Azizian, M. Ganjian, L. E. Fratila-Apachitei and A. A. Zadpoor, *Acta Biomater.*, 2019, **83**, 29–36.
68 Y. Xue, H. Xiao and Y. Zhang, *Int. J. Mol. Sci.*, 2015, **16**, 3626.
69 K. I. Ajoku, C. L. Wiatr and P. C. Miller, *Eur. Pat.*, EP1098566A1, 2001.
70 T. Vitanov and A. Popov, *J. Electroanal. Chem. Interfacial Electrochem.*, 1983, **159**, 437–441.
71 S. Ahrland, J. Chatt and N. R. Davies, *Q. Rev. Chem. Soc.*, 1958, **12**, 265–276.
72 Q. L. Feng, J. Wu, G. Q. Chen, F. Z. Cui, T. N. Kim and J. O. Kim, *J. Biomed. Mater. Res.*, 2000, **52**, 662–668.

73 M. N. Hasan, T. K. Maji, U. Pal, A. Bera, D. Bagchi, A. Halder, S. A. Ahmed, J. H. Al-Fahemi, T. M. Bawazeer, T. Saha-Dasgupta and S. K. Pal, *RSC Adv.*, 2020, **10**, 38890–38899.
74 A. Kubacka, M. S. Diez, D. Rojo, R. Bargiela, S. Ciordia, I. Zapico, J. P. Albar, C. Barbas, V. A. P. Martins Dos Santos, M. Fernández-García and M. Ferrer, *Sci. Rep.*, 2014, **41**, 4134.
75 S. Sarina, E. R. Waclawik and H. Zhu, *Green Chem.*, 2013, **15**, 1814–1833.
76 P. K. Stoimenov, R. L. Klinger, G. L. Marchin and K. J. Klabunde, *Langmuir*, 2002, **18**, 6679–6686.
77 S. Parham, D. H. B. Wicaksono, S. Bagherbaigi, S. L. Lee and H. Nur, *J. Chin. Chem. Soc.*, 2016, **63**, 385–393.
78 K. Sunada, Y. Kikuchi, K. Hashimoto and A. Fujishima, *Environ. Sci. Technol.*, 1998, **32**, 726–728.
79 C. Hu, Y. Lan, J. Qu, X. Hu and A. Wang, *J. Phys. Chem. B*, 2006, **110**, 4066–4072.
80 T. S. Wu, K. X. Wang, G. D. Li, S. Y. Sun, J. Sun and J. S. Chen, *ACS Appl. Mater. Interfaces*, 2010, **2**, 544–550.
81 Y. Ma, L. Tao, S. Bai and A. Hu, *Catalysts*, 2021, **11**, 1499.
82 R. Pachaiappan, S. Rajendran, P. L. Show, K. Manavalan and M. Naushad, *Chemosphere*, 2021, **272**, 128607.
83 P. P. Fu, Q. Xia, H. M. Hwang, P. C. Ray and H. Yu, *J. Food Drug Anal.*, 2014, **22**, 64–75.